UC-34
Issued: September 1976

Bremsstrahlung-Induced K Fluorescence

by

Ellery Storm

los alamos
scientific laboratory
of the University of California
LOS ALAMOS, NEW MEXICO 87545

An Affirmative Action/Equal Opportunity Employer

UNITED STATES
ENERGY RESEARCH AND DEVELOPMENT ADMINISTRATION
CONTRACT W-7405-ENG. 36

Printed in the United States of America. Available from
National Technical Information Service
U.S. Department of Commerce
5285 Port Royal Road
Springfield, VA 22161
Price: Printed Copy $4.00 Microfiche $2.25

BREMSSTRAHLUNG-INDUCED K FLUORESCENCE

by

Ellery Storm

ABSTRACT

Bremsstrahlung radiation can be used to excite nearly monoenergetic x rays in secondary targets, which are then used to study the energy response of radiation detectors if the intensity and purity are known. A method is suggested for calculating the spectral intensity of the secondary target radiation, including K-fluorescent x rays, and the bremsstrahlung and characteristic line radiation scattered from the target. Coherent and incoherent scatter are included in the calculation.

To test the theory, bremsstrahlung radiation from an x-ray unit operating in the 100- to 300-kV potential range was used to excite K-fluorescent radiation in secondary targets that range in atomic number from 29 to 90. The primary and secondary spectra were measured with NaI, silicon, and germanium detectors. The measured primary spectral intensities were used as input to the secondary spectral intensity calculation. Calculated secondary spectra were within 20% agreement with measurement.

Optimization of the secondary target intensity and purity is discussed as a function of target thickness, potential, and selective filtration.

I. INTRODUCTION

K-fluorescent x rays excited in a secondary target by photons from the primary target of an x-ray tube have been used to obtain monoenergetic sources in the 1- to 100-keV energy range.[1-3] Fluorescent sources, which have been used for microradiography of histologic sections[4] and for metallurgical microradiography,[5] have found widespread use in energy response measurements of radiation detectors[6-13] and as a method of elemental analysis.[14] The radiation emitted by the secondary target consists not only of K-fluorescent x rays but also includes the scattered bremsstrahlung contaminant. Consequently, in most applications, one is interested in the purity of the beam as well as the absolute intensity of the K-fluorescent x rays. Purity is defined as the ratio of K photons to total number of photons integrated over the energy spectrum. Purity and intensity can be measured with a photon spectrometer, but it would be useful and of theoretical interest to be able to calculate the spectrum and learn how to adjust the variables to optimize purity and intensity. However, one must first know the primary target spectrum, including both the bremsstrahlung continuum and the characteristic line radiation, to calculate the secondary target spectrum.

In this report, the primary target bremsstrahlung and characteristic line radiation are measured, and a method is suggested for calculating the secondary target K fluorescence and scattered bremsstrahlung

and characteristic line radiation. To test its validity, the method was applied to a specific case. A commercial x-ray unit with a tungsten-target tube was used as the primary source. With the x-ray tube operating in the 100- to 300-kV range, intensity as a function of photon energy was measured with a photon spectrometer. Secondary targets, varying in atomic number from 29 to 90, were irradiated by the primary source in a fixed geometry. Radiation from the secondary target was also measured with a photon spectrometer and the results were compared with the calculated spectra.

Measurements of the primary target radiation have been reported.[15] This report describes the secondary target spectral measurements, discusses the method of calculating the K fluorescence and scattered bremsstrahlung and characteristic line radiation, and compares the measurements with calculations. Coherent and incoherent scattering are included in the calculations. K-fluorescent intensity and purity are studied as a function of excitation potential, target thickness, and atomic number.

II. MEASUREMENT

A. Primary Target Radiation

The primary source was a constant-potential North American Philips Company Norelco MG-300 industrial x-ray unit containing an oil-immersed Müller Mö 301/10 tube. The tungsten target was at a 22° angle from the central ray and projected a 5-mm-square focal spot. The accelerating potential could be varied from 100 to 300 kV and the current from 2 to 10 mA. The Müller tube had a relatively large amount of inherent filtration, consisting of 0.44 g/cm^2 beryllium, 0.65 g/cm^2 Pyrex, 1.4 g/cm^2 oil, and 0.71 g/cm^2 Araldit plastic.

With the Norelco x-ray unit operating at 100, 150, 200, 250, and 300 kV, spectral measurements were made with silicon and germanium semiconductors and a NaI scintillator.[15] Because each detector distorts a spectrum differently, it was necessary to use H. I. Israel's program[16] to obtain a representation of the undistorted spectra. After estimating the undistorted spectrum, the program uses Monte Carlo techniques to distort the spectrum in the same manner as a detector of specified composition, geometry, and resolution.

A first estimate of the undistorted spectra was obtained from theoretical considerations.[17,18] The first estimate was distorted by the Israel program, compared to measurement, then revised to bring it more nearly into agreement with measurement. The second estimate was distorted by the program and then compared to measurement. Further revisions were made, and the process was repeated until satisfactory agreement with measurement was achieved.

Figure 1 shows the final estimate of the undistorted spectra, which agree within 10% with the spectral measurements obtained with all three detector types. Because the K-lines and K-edge discontinuity were present in the first estimate derived from theory, these same features appear in the undistorted spectra. The spectra in Fig. 1 are free of detector attenuation and distortion but are attenuated by inherent filtration. These spectral distributions are taken to represent the true primary spectral distribution incident on the secondary fluorescent targets.

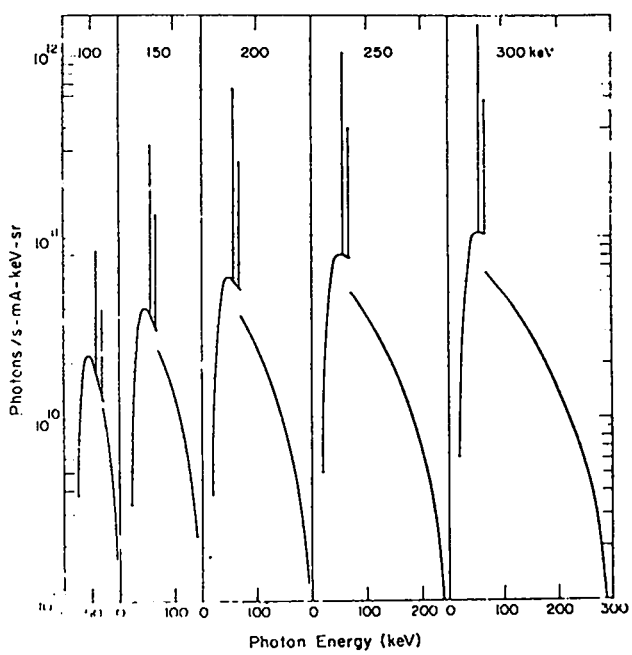

Fig. 1.
Undistorted "measured" spectra.

B. Secondary Target Radiation

1. Experimental Arrangement and Procedure. Figure 2 shows the arrangement for irradiating the secondary targets to produce K-fluorescent radiation. The primary source was the Norelco unit described above. Except for the exit window, the tube head was completely encased in a 2.5-cm-thick lead shield mounted vertically on a turntable. A beam-limiting lead diaphragm with a tapered conical hole was attached to the exit window. Positioned against the exit window diaphragm was a lead-lined brass cylinder that served as a holder for the secondary targets and also absorbed the transmitted primary beam. The targets were placed in the primary beam through a slit in the top of the cylinder. The secondary target, with its center 15 cm from the primary target, was at a 45° angle to the central ray of the primary beam. The K-fluorescent beam passed through a 2.2-cm hole in the brass cylinder. An electrically actuated shutter in front of the first diaphragm permitted the fluorescent beam to be stopped without turning off power to the x-ray tube. A 3.0-cm-diam beam-limiting diaphragm was located 8 cm from the first diaphragm. Aluminum filters were placed over this second diaphragm to absorb L x rays produced in the targets.

Table I lists the 10 targets and their thicknesses. The targets were cut or pressed into 5-cm-diam disks. Target thicknesses were at least 1 mfp thick for their K x rays. K radiation was assumed to consist of two lines with the combined weighted average of K_α plus K_β energies. The filters used to absorb the L lines produced in the target are also given in the table. K lines produced in the lighter elements of the compounds were <3 keV and were absorbed by the aluminum filters.

Spectra from the secondary target were measured with essentially the same arrangement used with the primary target (Fig. 3). Detectors were located 49 m from the targets with an evacuated Orangeburg pipe between the source and detector. The ends of the pipe were covered with 0.0105-g/cm^2-thick Mylar windows. Air between the secondary target and first Mylar window, air in the pipe, and air between the second Mylar window and detector totaled 0.047 g/cm^2 in thickness. The silicon, germanium, and NaI detectors used in the primary target measurements were also used in the secondary target measurements. Each of these detectors distorts an x-ray spectrum differently, and each has its advantages and limitations; these will be discussed when the experimental results are presented.

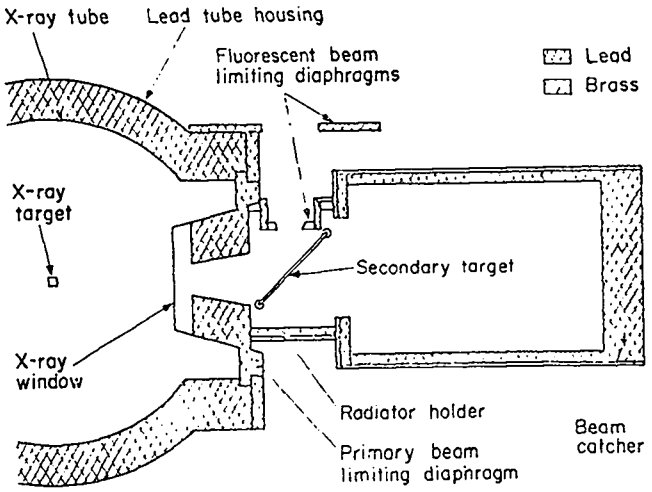

Fig. 2.

Arrangement for irradiating secondary targets to produce K-fluorescent radiation.

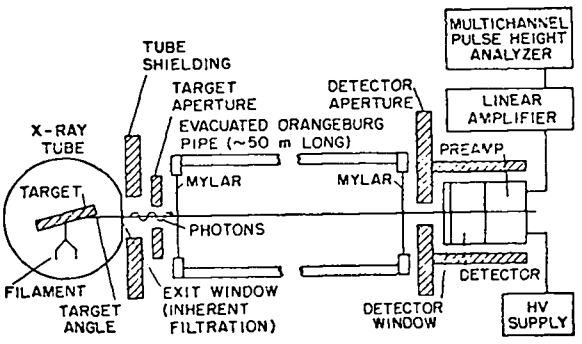

Fig. 3.

Experimental arrangement for the measurement of x-ray spectra.

TABLE I

K-LINE ENERGIES, THICKNESSES, AND L-LINE ABSORBERS OF SECONDARY TARGETS

Z	Target Material	Target Thickness (g/cm^2)[a]	K_α (keV)	K_β (keV)	K^b (keV)	Al L X-Ray Absorber (g/cm^2)
29	Cu	0.023	8.041	8.907	8.136	0.006
35	NaBr	0.13	11.907	13.300	12.087	0.055
42	Mo	0.052	17.443	19.648	17.781	0.055
47	Ag	0.074	22.103	25.008	22.581	0.103
56	BaS	0.43	32.062	36.535	32.890	0.103
64	Gd_2O_3	0.53	42.750	48.918	43.949	0.103
70	Yb_2O_3	0.88	52.014	59.652	53.542	0.441
77	Ir	1.4	64.303	73.919	66.296	0.441
82	Pb	0.72	74.159	85.370	76.539	0.441
90	Th	1.3	92.050	106.169	95.144	1.45

[a] Includes mass of lighter elements in compounds.

[b] Combined weighted average of K_α and K_β.

The Technical Measurements Corporation (TMC) photon spectroscopy system included a lithium-drifted silicon detector, a cryogenic chamber, an ion pump with power supply, and a 10-ℓ liquid nitrogen reservoir. The silicon disk was 0.3 cm thick and 1.27 cm in diameter with a 0.5-μm-thick dead layer. A 0.025-cm-thick beryllium window was mounted in the cryogenic chamber parallel to the plane of the detector so that entering photons were normal to the surface. The first stage of the TMC preamplifier was inside the cryogenic chamber at liquid nitrogen temperature, and its output signal was fed to an Ortec model 410 amplifier.

The disk-shaped lithium-drifted germanium detector, Ortec Company model 8047, was 0.75 cm thick and 2.28 cm in diameter with an active area of 4 cm^2. It was encapsulated in an aluminum cryostat that rested vertically in a 25-ℓ Dewar of liquid nitrogen. A 0.046-g/cm^2-thick beryllium window in the cryostat was aligned with the side of the detector, i.e., photons were incident on the cylindrical surface of the disk, rather than on one of the plane surfaces. Consequently, the germanium dead layer was <0.0025 cm. The detector was coupled to an uncooled Los Alamos Scientific Laboratory (LASL) model 580 preamplifier and an Ortec model 410 linear amplifier.

The Harshaw Chemical Company model 12S12 detector was a 7.6-cm-diam by 7.6-cm-deep cylindrical thallium-activated NaI crystal, optically coupled by a quartz light pipe to an RCA model 8054 photomultiplier tube; the entire unit was contained in a 0.274-g/cm^2-thick aluminum can. Its output signal was fed to a Victoreen Instrument Company preamplifier model SPA-C and amplifier model SA-1.

The detectors were completely shielded except for their windows and rested against the detector aperture. Alignment was made both optically and by intensity measurements. Background was subtracted with the x-ray unit on and with the shutter over the fluorescent source.

Pulse height analysis of all spectra was performed with a Victoreen Scipp 400-channel analyzer that was housed with the amplifiers and output equipment in a small trailer near the detector. The

analyzer gain was set so that one channel width corresponded to a 1-keV interval. This setting was checked daily before and after each run, and it was seldom necessary to adjust the fine gain. Gamma-ray emitting isotopes were used to calibrate the spectrometer. These included the 22-keV ^{109}Cd line, the 60-keV ^{241}Am line, the 122-keV ^{57}Co line, and the 279-keV ^{203}Hg line.

Spectral measurements were made with the x-ray unit operating at 100, 200, and 300 kV. Because the secondary target intensities were considerably smaller than the primary target intensities, increased tube currents, longer counting times, and larger detector apertures were used to measure the fluorescent spectra. Table II gives tube currents, counting times, and detector aperture areas used with each operating potential and detector.

2. Results. Fluorescent spectral measurements are given in Figs. 4-12 in terms of counts per kiloelectron volt for the conditions listed in Table II and primary excitation potentials of 100, 200, and 300 kV. Measurement is shown by the actual data points, and theoretical results (described later) are shown by the solid line.

The spectra observed with the silicon detector are shown in Fig. 4 for copper, NaBr, and molybdenum targets. Of the three detectors, silicon had the best resolution but poorest efficiency.[16] The FWHM resolution was 1 and 2 keV at photon energies of 10 and 100 keV, respectively. As a result, the K lines are relatively narrow. However, the silicon efficiency curve falls rapidly above 20 keV, decreasing to 10% at 60 keV and to 2% at 100 keV. Thus, the contribution of the scattered spectrum to the total intensity appears to be insignificant.

The thicker and denser germanium detector was considerably more efficient than the silicon detector, and gave truer representation of the importance of the scattered spectrum. The germanium detector's efficiency was essentially 1.0 below 100 keV, and fell off rapidly at the higher energies. The germanium measurements are shown in Figs. 5-8. Resolution of the germanium detector was poorer than that of the silicon detector, being 2- and 3-keV FWHM at photon energies of 10 and 100 keV, respectively. The K_α and K_β lines do not separate until Z = 64. Escape peaks appear 10 keV below the K lines. As can be seen from the measurements, the usefulness of the germanium detector was limited to energies >20 keV because of large detector leakage currents.

The NaI detector had the best efficiency, the poorest resolution, and the largest escape peaks of the three detectors (see Figs. 9-12). Resolution of the NaI detector was 4- and 10-keV FWHM at photon energies of 10 and 100 keV, respectively. Separation of the K_α and K_β lines does not occur even at Z = 90, although the presence of the K_β line is apparent

TABLE II

CONDITIONS FOR
FLUORESCENT SPECTRAL MEASUREMENTS

		Si and Ge Detectors[a]		NaI Detector[a]	
Potential (kV)	Current (mA)	Area (cm^2)	Time (s)	Area (cm^2)	Time (s)
100	15	0.114	3000	2.85	600
200	10	0.114	1800	2.85	360
300	10	0.114	1220	2.85	246

[a]Source-to-detector distance = 4900 cm.

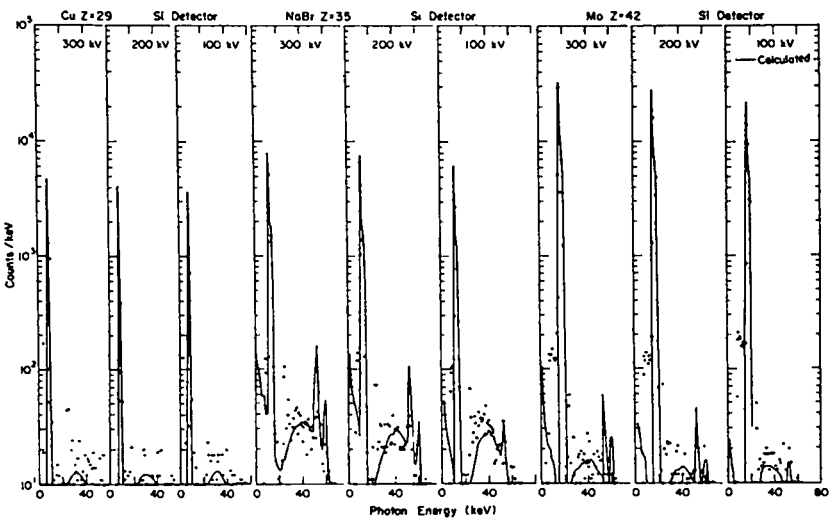

Fig. 4.
Silicon-measured copper, NaBr, and molybdenum spectra.

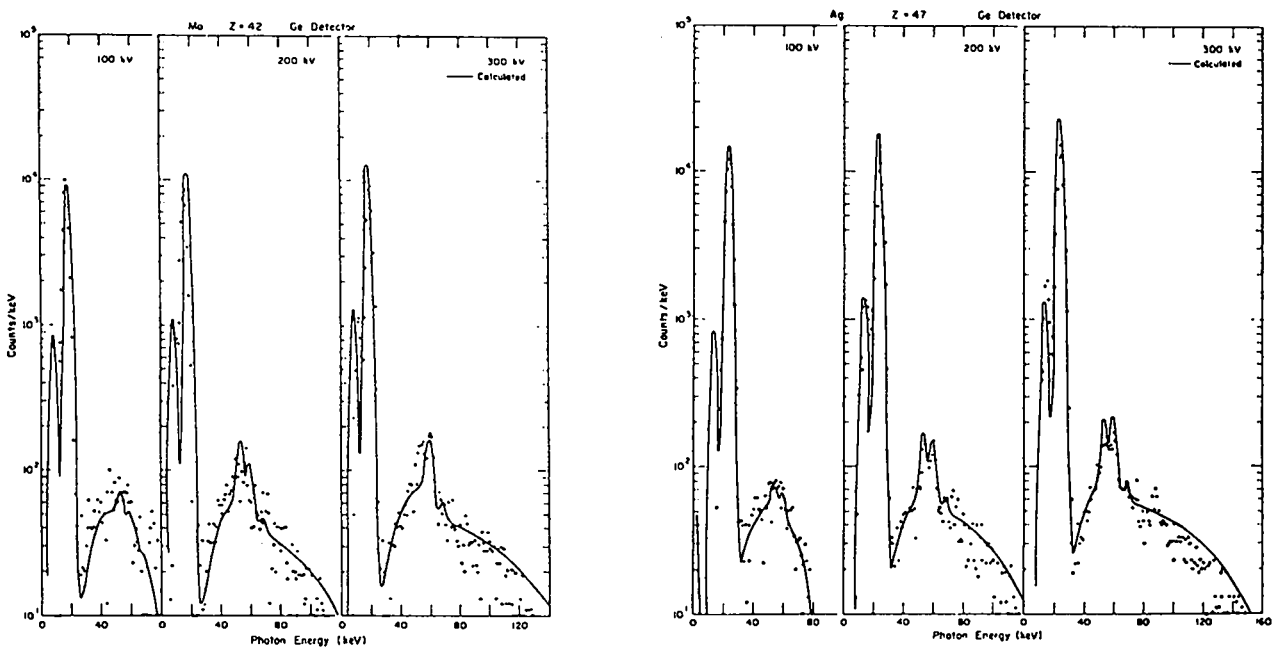

Fig. 5.
Germanium-measured molybdenum and silver spectra.

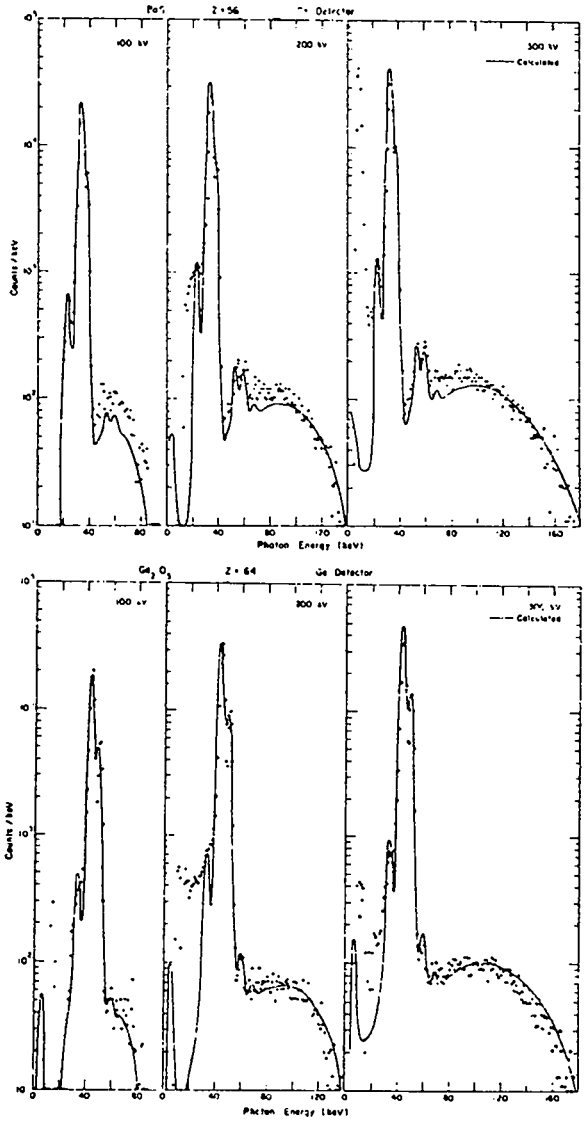

Fig. 6.
Germanium-measured BaS and Gd_2O_3 spectra.

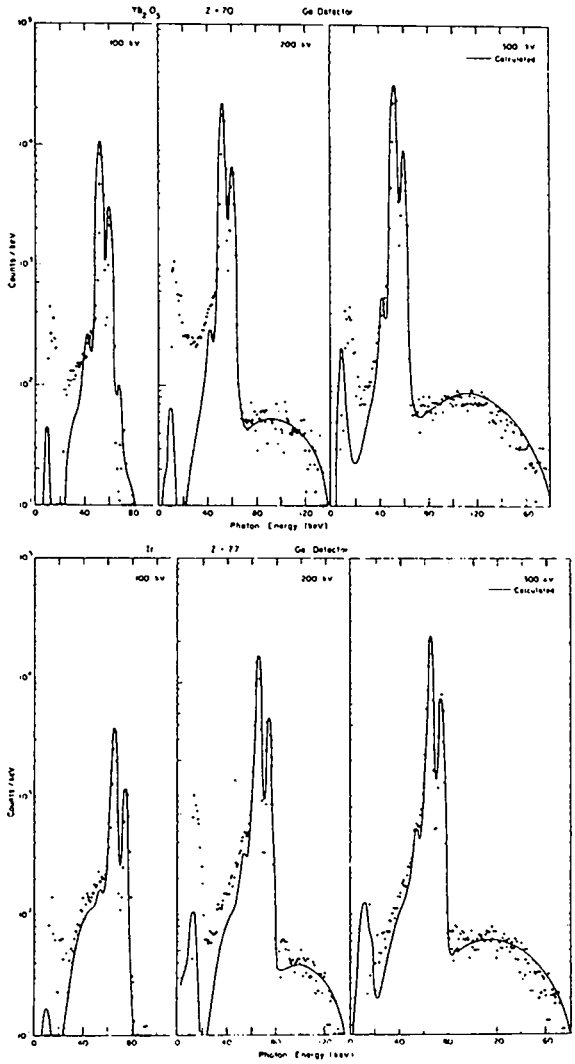

Fig. 7.
Germanium-measured Yb_2O_3 and iridium spectra.

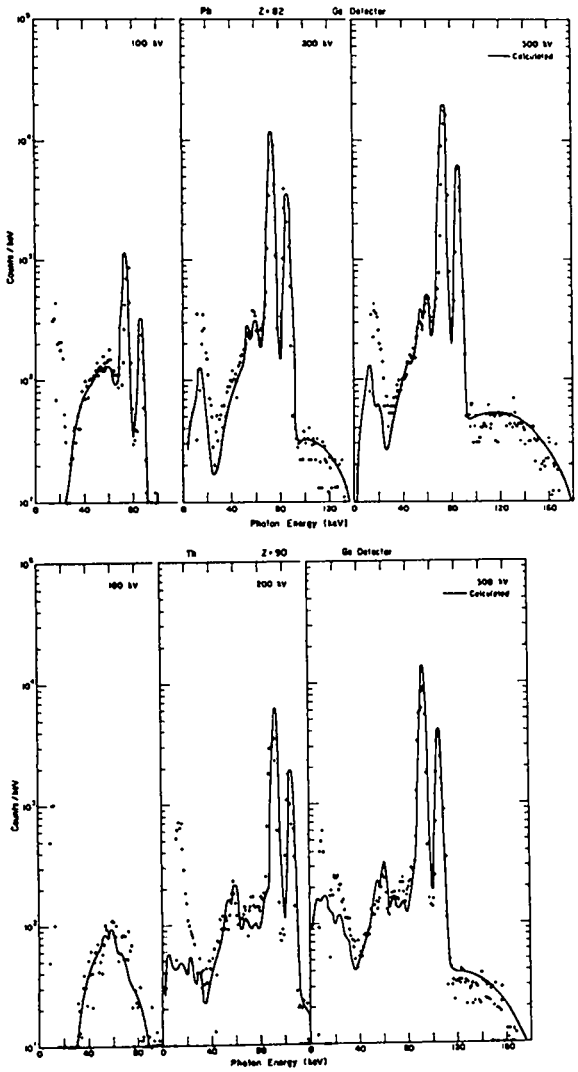

Fig. 8.

Germanium-measured lead and thorium spectra.

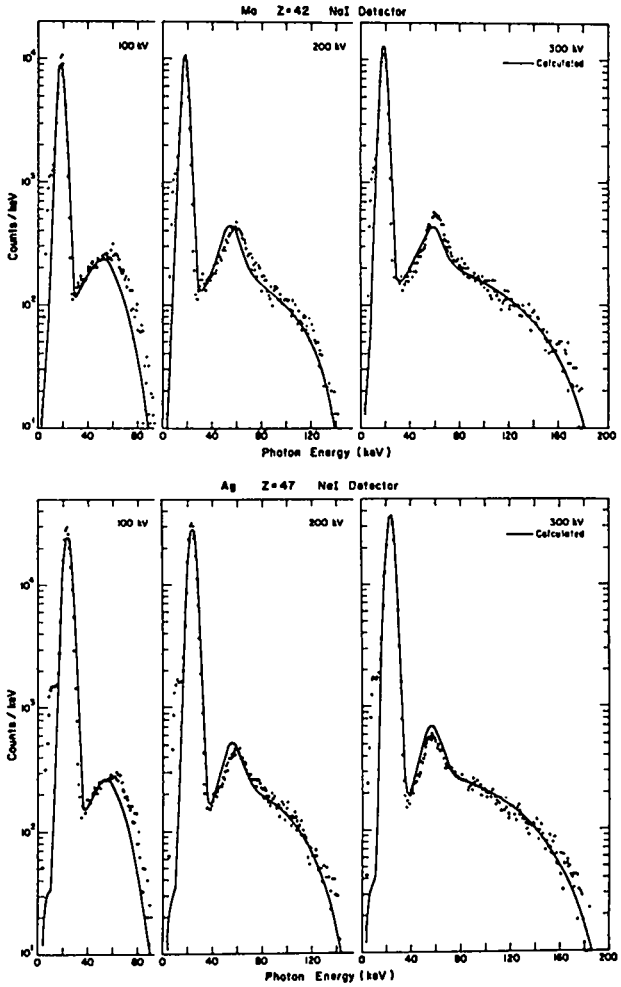

Fig. 9.

NaI-measured molybdenum and silver spectra.

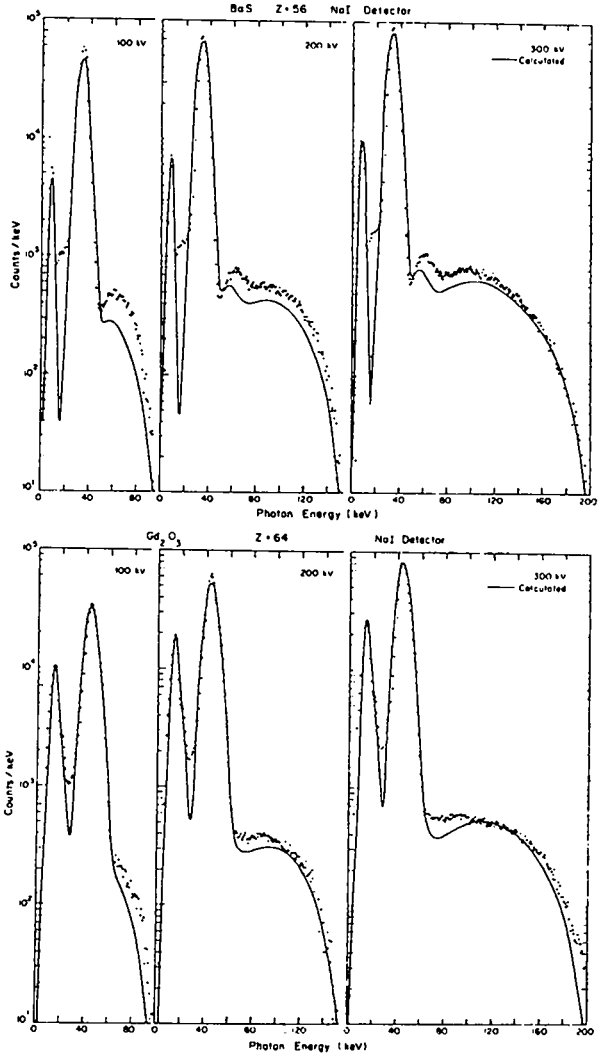

Fig. 10.
NaI-measured BaS and Gd_2O_3 spectra.

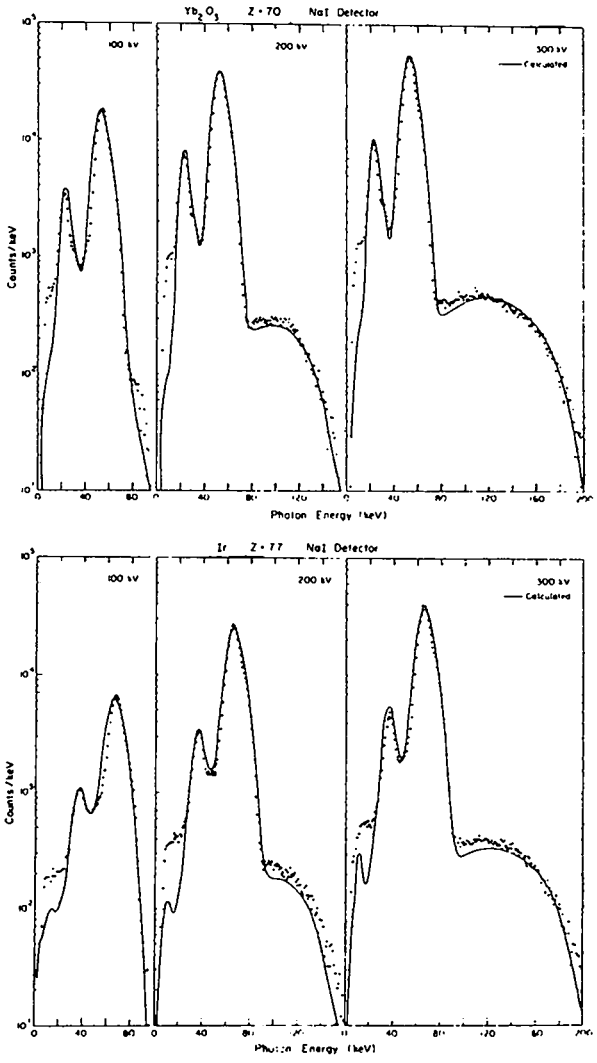

Fig. 11.
NaI-measured Yb_2O_3 and iridium spectra.

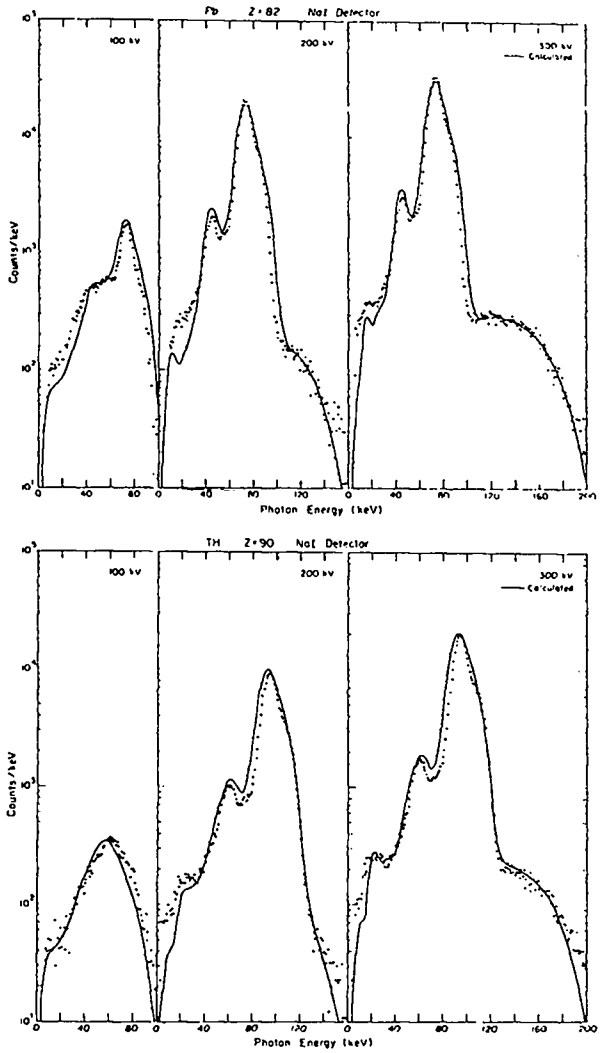

Fig. 12.
NaI-measured lead and thorium spectra.

above Z = 56 from the nonGaussian distribution of the photopeak. Above Z = 56 the escape peaks also appear ~30 keV below the K lines. Because the NaI efficiency was 0.9 at 300 keV, the NaI spectra give the clearest representation of the scattered spectrum.

In the spectral measurements shown in Figs. 4-12, the target thicknesses (Table I) were held constant and the primary potential varied. In the spectral measurements, shown in Figs. 13 and 14, the potential was held constant at 250 kV and the target thicknesses were varied. Spectra obtained with three different thicknesses of copper, molybdenum, gadolinium, and lead foils using the various detectors are shown in Figs. 13 and 14.

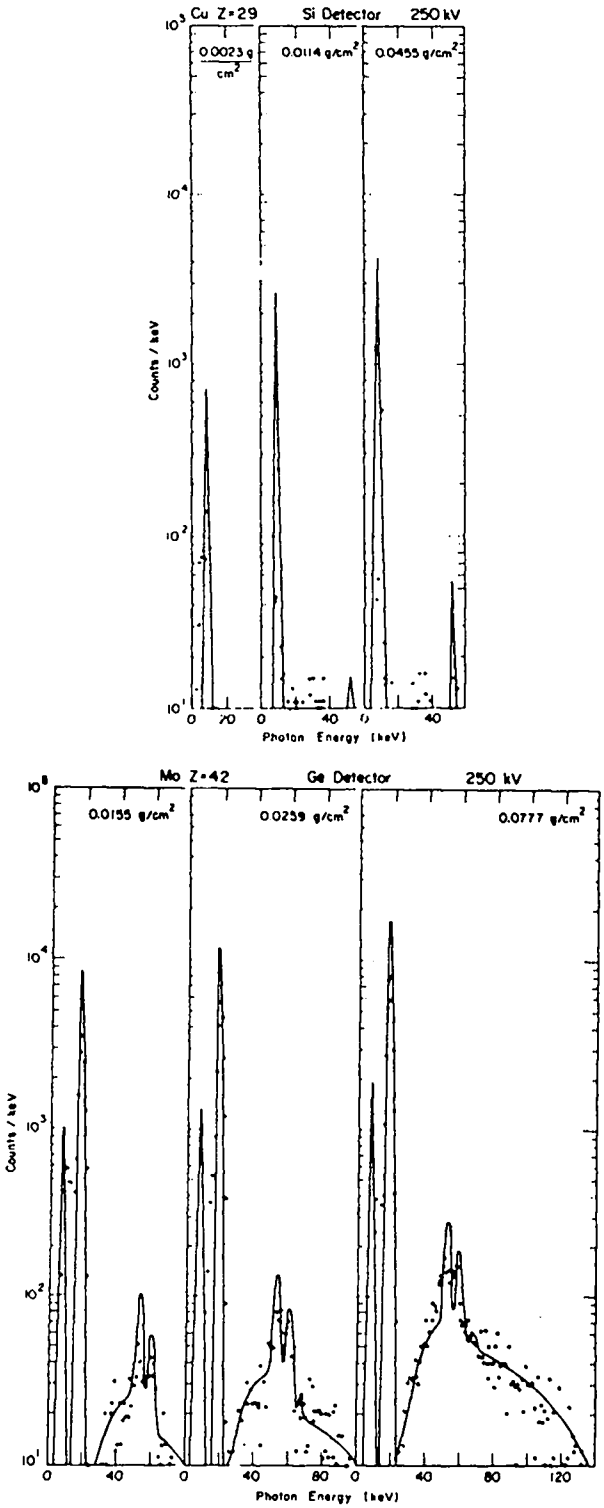

Fig. 13.
Silicon-measured copper and germanium-measured molybdenum spectra with target thickness varied.

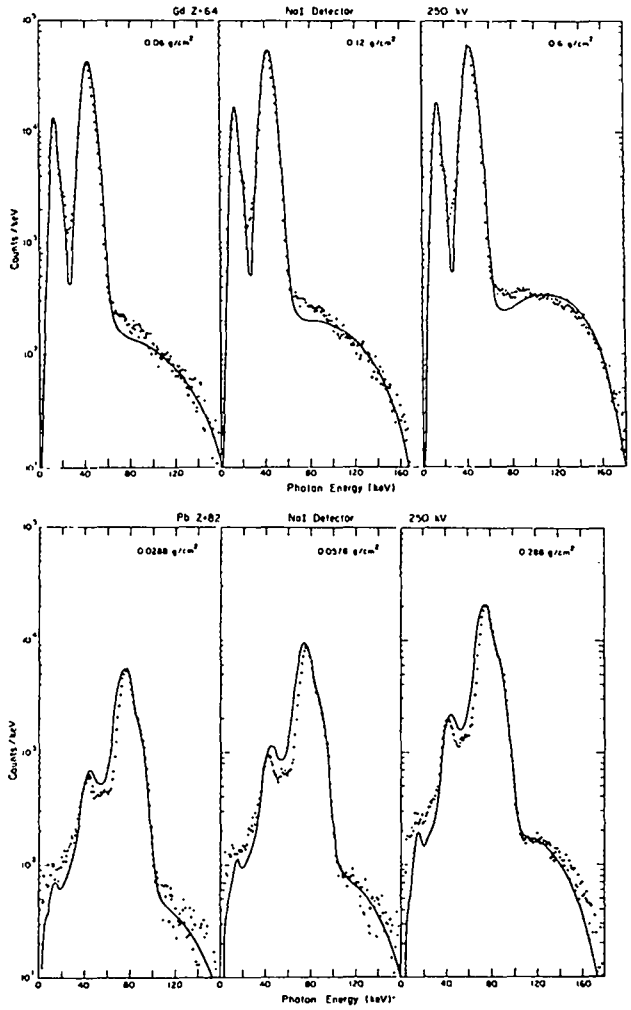

Fig. 14.
NaI-measured gadolinium and lead spectra with target thickness varied.

3. Previous Measurements. There have been many papers[1-13] describing the use of a primary x-ray source to excite fluorescent K radiation in secondary targets. The geometry used for this report is designed primarily for use in the calibration of radiation detectors. For example, the equipment described here has been used to measure the photon energy response of instruments used in personnel dosimetry, health physics surveys, radiation laboratory measurements, x-ray astronomy, and nuclear-device tests. Descriptions of similar calibration facilities at Battelle Memorial Institute,[8,10] Lawrence Livermore Laboratory,[6,7] and EG&G Las Vegas Division[11] have been reported.

The 200-kV Battelle facility was first described by Larson et al.[10] without spectral measurements, but later Kathren et al.[8] presented fluorescent spectral measurements for six metallic targets with atomic numbers from 40 to 92 and primary voltages of 60 to 140 kV. The measurements were in terms of relative intensity and indicated more low-energy scatter than was found in the present measurements, probably because of the much thinner inherent filtration in Battelle's primary x-ray tube.

Livermore used three separate x-ray units with maximum operating potentials of 75, 150, and 400 kV to obtain fluorescent x rays from 22 targets varying in atomic number from 29 to 92. Gaines et al.[6] presented a catalog of fluorescent spectral measurements with and without prefilters (which reduce low-energy scatter) and postfilters (which preferentially attenuate K_β lines to obtain purer K_α lines). The spectra were presented in figures without numerical values for either intensity or photon energy.

The EG&G reports[11] described a 75-kV x-ray unit used to obtain fluorescent x rays. Spectral measurements were given for 11 targets in terms of relative intensity. The measurements made by Battelle and EG&G indicated more low-energy scatter than the present measurements because of thinner inherent filtration.

In effect, there do not appear to be any measurements that can be directly compared with the secondary-target spectral measurements given here. In addition, no attempt seems to have been made to predict the secondary target spectra theoretically.

III. Theory

A. Geometry Assumed in the Calculation.

The geometry of the experimental arrangement is shown in Fig. 15. Photons from the primary target pass through the beam-limiting aperture and strike the secondary target, which is inclined at a 45° angle to the central ray of the primary beam. Distances from the primary target to the beam-limiting aperture and to the center of the secondary target are r_t and r_r, respectively. The area of the beam-limiting diaphragm and the area of the secondary target irradiated by the primary beam are A_t and A_r, respectively.

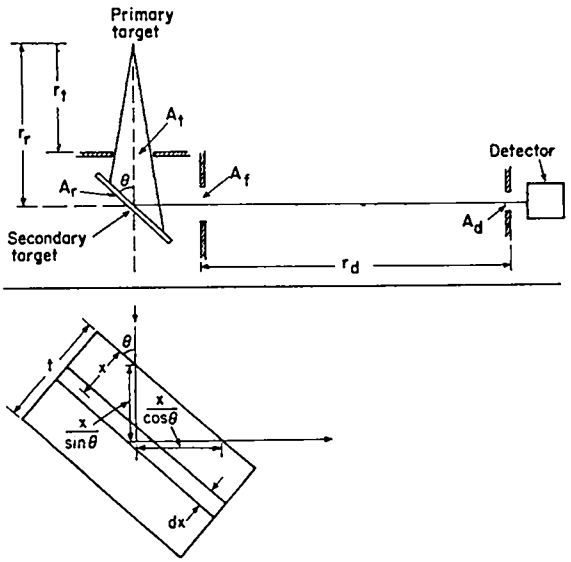

Fig. 15.
Geometry used in spectral measurements.

Because each point on the secondary target is not the same distance from the primary target, the target is irradiated nonuniformly. At the secondary target position, the irradiated area is elliptical. Along the major axis, the point closest to the primary target is the most intense and the point farthest is the least intense. However, because the most intense point is farthest and the least intense point closest to the fluorescent diaphragm of area A_f, the intensity is essentially uniform at the diaphragm when the target is oriented 45° with respect to the primary beam. In effect, the geometry results in a uniform 2.2-cm-diam circular source located at the fluorescent diaphragm.

Films placed at various distances from the fluorescent diaphragm showed that the intensity was uniform over a circular region and fell off gradually at the edges. The diameter d_f of the central uniform region was proportional to source-to-detector distance r_d and was given by $d_f = 0.08\, r_d$ for $r_d > 15$ cm. Ionization chamber measurements demonstrated that for distances > 15 cm, the inverse square law was obeyed within 2% if distances were measured from the fluorescent diaphragm to the detector.

Referring once more to Fig. 15, the primary beam produces K-fluorescent radiation in the secondary target, and scatters both incoherently and coherently from the target. The K and scattered photons pass through the fluorescent diaphragm, area A_f, and are measured by the detector with aperture area A_d, located a distance r_d from the fluorescent diaphragm. The photons emitted from the target are observed at a 90° angle to the central ray of the primary beam.

B. Primary Intensity Inside the Target

As mentioned earlier, the undistorted "measured" spectra shown in Fig. 1, which include inherent filtration, will be assumed in the following calculation to represent the primary spectral distributions, referred to as $I_{primary}$ and given in units of photons/s-mA-keV-sr.

From Fig. 15, the solid angle subtended by the secondary target is A_t/r_t^2. The total target area irradiated at distance r_r is $A_r = (A_t/\sin\theta)(r_r^2/r_t^2)$. Hence, the photon intensity per unit area incident on the target is

$$I_{incident} = I_{primary} \left[\frac{A_t}{r_t^2}\right]\left[\frac{\sin\theta}{A_t}\frac{r_t^2}{r_r^2}\right] = I_{primary}\ \frac{\sin\theta}{r_r^2}\ , \qquad (1)$$

where $I_{incident}$ is in units of photons/s-mA-keV-cm^2.

The intensity of the incident beam at a point x in the target is

$$I_x = I_{incident}\ \exp\{-\mu_k x/\sin\theta\}\ , \qquad (2)$$

where μ_k is the total attenuation coefficient of the incident photons with energy k, and $x/\sin\theta$ is the distance traveled by the photons inside the target to reach point x.

The decrease in incident beam intensity in passing through an infinitesimal layer dx is, by differentiating Eq. (2),

$$dI_x = -I_{incident}\ (\mu_k x/\sin\theta)$$

$$\chi\ \exp\{-\mu_k x/\sin\theta\}\ dx\ . \qquad (3)$$

If $dI_{interaction} = -dI_x$ is the intensity of the photons interacting in the layer dx, then from Eq. (1) the interaction intensity in terms of $I_{primary}$ is

$$dI_{interaction} = (I_{primary}/r_r^2)\ \mu_k$$

$$\chi\ \exp\{-\mu_k x/\sin\theta\}\ dx\ . \qquad (4)$$

In the energy region of interest, $10 \le k \le 300$ keV, the total attenuation coefficient is the sum of the photoelectric (τ_k), coherent (σ_{coh}), and incoherent (σ_{inc}) coefficients, i.e.,

$$\mu_k = \tau_k + \sigma_{coh} + \sigma_{inc}\ . \qquad (5)$$

Hence, the photon interaction intensity can be written as the sum of three terms.

$$dI_{interaction} = (I_{primary}/r_r^2)$$
$$\chi\ \Big[\tau_k\ \exp\{-\mu_k x/\sin\theta\}$$
$$+\ \sigma_{coh}\ \exp\{-\mu_k x/\sin\theta\}$$
$$+\ \sigma_{inc}\ \exp\{-\mu_k x/\sin\theta\}\Big]\ dx. \qquad (6)$$

C. K Photons

K_α- and K_β-photon intensities can be calculated from the first term in Eq. (6). The photoelectric coefficient, τ_k, represents the probability of a photon interaction occurring in any of the atomic shells. If σ_K/σ_T is the ratio of K shell to total shell interactions, then $(\tau_k)(\sigma_K/\sigma_T)$ is the probability of a photon interacting only with atomic K shells. Of the photons interacting with atomic K shells, only a fraction produce K_α photons. If ω_K is the ratio of K photons produced to K-shell interactions and K_α/K_T is the ratio of K_α to total K photons produced, then the probability of photons with energy k producing K_α photons is $(\tau_k)(\sigma_K/\sigma_T)\ (\omega_K)(K_\alpha/K_T)$.

From the layer dx, K_α photons travel a distance $x/\cos\theta$ before leaving the target. Hence, they are attenuated by a factor $\exp[-\mu_{K_\alpha} x/\cos\theta]$, where μ_{K_α} is the total attenuation coefficient of a photon with energy K_α.

Only the fraction of the photons leaving the target and directed toward the detector are recorded. Because the K_α photons are emitted isotropically, only $1/4\ \pi$ reach the detector. The area seen by the detector is $A_f/\sin\theta$, where A_f is the area of the fluorescent diaphragm.

Thus the K_α-photon intensity leaving the target in the direction of the detector from the layer dx is

$$dI_{K_\alpha} = (I_{primary}/r_r^2)\ (A_f/\sin\theta)$$
$$\chi\ (1/4\pi)\left[\frac{K_\alpha}{K_T}\,\omega_K\,\frac{\sigma_K}{\sigma_T}\right]\tau_k$$
$$\chi\ \exp\{-\mu_k x/\sin\theta - \mu_{K_\alpha} x/\cos\theta\}$$
$$\chi\ dx\ . \qquad (7)$$

Integration over the total thickness t of the target with $\theta = 45°$ gives

$$I_{K_\alpha} = I_{primary}\,(A_f/r_r^2) \times \left[\frac{K_\alpha}{K_T}\,\frac{\omega_K}{4\pi}\,\frac{\sigma_K}{\sigma_T}\right] \frac{\tau_k}{\mu_k + \mu_{K_\alpha}} \times \left[1 - \exp\{-\sqrt{2}(\mu_k + \mu_{K_\alpha})t\}\right]. \quad (8)$$

However, K_α photons are produced only by photons in the incident spectrum with energies between k_K, the K-edge energy, and $k_o = T_o$, the maximum photon energy or the accelerating potential of the primary x-ray tube. Thus, the K_α-photon intensity produced by photons with energy $k_K \leq k \leq k_o$ and emitted from the target is

$$I_{K_\alpha} = \left[\frac{K_\alpha}{K_T}\,\frac{\omega_K}{4\pi}\,\frac{\sigma_K}{\sigma_T}\right] (A_f/r_r^2) \times \int_{k_K}^{k_o} I_{primary}\,\frac{\tau_k}{\mu_k + \mu_{K_\alpha}} \times \left[1 - \exp\{-\sqrt{2}(\mu_k + \mu_{K_\alpha})t\}\right] \times dk\,. \quad (9)$$

Similarly, the K_β-photon intensity emitted from the target is

$$I_{K_\beta} = \left[\frac{K_\beta}{K_T}\,\frac{\omega_K}{4\pi}\,\frac{\sigma_K}{\sigma_T}\right] (A_f/r_r^2) \times \int_{k_K}^{k_o} I_{primary}\,\frac{\tau_k}{\mu_k + \mu_{K_\beta}} \times \left[1 - \exp\{-\sqrt{2}(\mu_k + \mu_{K_\beta})t\}\right] \times dk\,. \quad (10)$$

where I_{K_α} and I_{K_β} are in units of photons/s-mA-sr.

The numerical values used in this calculation for ω_K, σ_K/σ_T, K_α/K_T, K_β/K_T, μ_{K_α}, and μ_{K_β} are listed in Table III. Photoelectric τ_k and total μ_k attenuation coefficients are given in Tables IV and V, respectively. The fluorescent diaphragm area A_f was 3.80 cm^2 and the primary to secondary target distance r_r was 15 cm.

D. Coherently Scattered Photons

The coherently scattered photon intensity can be calculated from the second term in Eq. (6). The coherent scattering coefficient σ_{coh} represents the probability of a coherent interaction occurring, summed over all angles of photon emission. Figure 15 shows that only photons leaving the secondary target at a 90° angle to the incident beam are recorded by the detector. Therefore, σ_{coh} must be replaced by $d\sigma_{coh}/d\Omega$, which represents the probability that a photon with energy k will interact coherently in the layer dx and a scattered photon will emerge in the direction of the detector within the solid angle $d\Omega$.

In Rayleigh or coherent scatter, a photon with energy k interacts with atomic electrons and is reradiated with the same energy k. Coherently scattered photons, produced in the layer dx, travel a distance $x/\cos\theta$ in reaching the surface of the target and are attenuated by a factor $\exp[-\mu_k x/\cos\theta]$. Thus the coherently scattered photon intensity leaving the target in the direction of the detector from layer dx is

TABLE III

CONSTANTS USED IN THE CALCULATION
OF SECONDARY TARGET RADIATION

Z	ω_K	$\frac{\sigma_K}{\sigma_T}$	$\frac{K_\alpha}{K_T}$	$\frac{K_\beta}{K_T}$	μ_{K_α} (cm^2/g)	μ_{K_β} (cm^2/g)	K-Edge Energy (keV)	K' Edge Energy (keV)
29	0.445	0.871	0.891	0.109	50.9	39.5	8.98	8.82
35	0.622	0.862	0.871	0.129	30.1	22.6	13.47	13.12
42	0.764	0.852	0.847	0.153	18.8	13.8	20.00	19.25
47	0.830	0.842	0.836	0.164	14.3	10.1	25.51	24.30
56	0.901	0.830	0.815	0.185	7.94	5.88	37.44	34.88
64	0.934	0.818	0.806	0.194	5.75	4.10	50.24	45.74
70	0.950	0.811	0.800	0.200	4.52	3.13	61.33	54.76
77	0.962	0.797	0.792	0.208	3.51	2.40	76.11	66.24
82	0.968	0.788	0.788	0.212	2.91	2.01	88.00	75.07
90	0.975	0.772	0.781	0.219	2.21	1.56	109.65	90.28

Z	K_α Energy (keV)	K'_α Energy (keV)	K_β Energy (keV)	K'_β Energy (keV)	K-Edge Energy (keV)	K'-Edge Energy (keV)
74	58.83	52.76	67.56	59.67	69.52	61.20

Target	μ_{K_α} (cm^2/g)	μ_{K_β} (cm^2/g)
NaBr	25.4	19.0
BaS	6.76	5.00
Gd_2O_3	5.02	3.59
Yb_2O_3	3.99	2.77

TABLE IV

SECONDARY TARGET PHOTOELECTRIC COEFFICIENTS (τ_k)

k (keV)	Cu (cm^2/g)	Br (cm^2/g)	Mo (cm^2/g)	Ag (cm^2/g)	Ba (cm^2/g)	Gd (cm^2/g)	Yb (cm^2/g)
8.98	283						
13.47		148					
20.00	33.0	51.6	81.0				
25.51				55.0			
30	10.3	16.9	27.3	35.8			
37.44					28.5		
40	4.48	7.54	12.4	16.6	23.9		
50	2.31	3.96	6.59	8.99	13.2		
50.24						18.0	
60	1.35	2.33	3.94	5.40	8.11	11.3	
61.33							13.1
70	0.853	1.51	2.54	3.52	5.44	7.66	9.22
76.11							
80	0.561	0.995	1.71	2.39	3.67	5.25	6.54
88.00							
90	0.393	0.701	1.19	1.69	2.65	3.79	4.73
100	0.284	0.509	0.891	1.25	1.96	2.84	3.58
109.65							
110	0.211	0.381	0.672	0.949	1.50	2.19	2.78
120	0.163	0.292	0.515	0.731	1.16	1.72	2.18
130	0.128	0.226	0.408	0.586	0.934	1.38	1.75
140	0.102	0.181	0.330	0.475	0.750	1.12	1.43
150	0.0826	0.148	0.272	0.387	0.627	0.938	1.20
160	0.0682	0.122	0.222	0.321	0.522	0.777	0.985
170	0.0569	0.103	0.187	0.270	0.439	0.659	0.849
180	0.0479	0.0867	0.158	0.229	0.384	0.555	0.731
190	0.0408	0.0739	0.135	0.195	0.320	0.479	0.626
200	0.0345	0.0637	0.117	0.168	0.276	0.406	0.546
210	0.0303	0.0550	0.100	0.147	0.244	0.364	0.477
220	0.0263	0.0482	0.0879	0.128	0.213	0.320	0.421
230	0.0229	0.0421	0.0766	0.113	0.189	0.283	0.376
240	0.0203	0.0372	0.0684	0.0999	0.168	0.253	0.338
250	0.0179	0.0329	0.0603	0.0877	0.150	0.228	0.301
260	0.0160	0.0294	0.0540	0.0787	0.135	0.205	0.271
270	0.0143	0.0264	0.0486	0.0703	0.121	0.186	0.245
280	0.0128	0.0237	0.0439	0.0636	0.110	0.169	0.223
290	0.0117	0.0216	0.0395	0.0575	0.0995	0.153	0.204

TABLE IV (cont)

k (keV)	Ir (cm^2/g)	Pb (cm^2/g)	Th (cm^2/g)	NaBr (cm^2/g)	BaS (cm^2/g)	Gd_2O_3 (cm^2/g)	Yb_2O_3 (cm^2/g)
8.98							
13.47				116			
20.00				40.5			
25.51							
30				13.2			
37.44					23.3		
40				5.90	19.5		
50				3.10	10.8		
50.24						15.6	
60				1.82	6.61	9.81	
61.33							11.5
70				1.18	4.54	6.65	8.10
76.11	9.21						
80	8.11			0.777	2.99	4.56	5.74
88.00		7.21					
90	5.98	6.83		0.547	2.16	3.29	4.15
100	4.54	5.23		0.397	1.60	2.46	3.14
109.65			4.98				
110	3.54	4.07		0.297	1.22	1.90	2.44
120	2.79	3.23	4.02	0.228	0.945	1.49	1.91
130	2.26	2.62	3.27	0.176	0.760	1.20	1.54
140	1.86	2.17	2.70	0.141	0.611	0.972	1.26
150	1.56	1.82	2.27	0.116	0.510	0.814	1.05
160	1.32	1.53	1.92	0.0952	0.425	0.674	0.865
170	1.12	1.30	1.63	0.0804	0.357	0.572	0.746
180	0.959	1.12	1.41	0.0677	0.312	0.482	0.642
190	0.827	0.965	1.23	0.0577	0.260	0.416	0.550
200	0.717	0.849	1.07	0.0497	0.225	0.362	0.480
210	0.636	0.744	0.942	0.0429	0.198	0.316	0.419
220	0.564	0.660	0.838	0.0376	0.173	0.278	0.370
230	0.501	0.590	0.747	0.0328	0.154	0.246	0.330
240	0.442	0.523	0.667	0.0290	0.137	0.220	0.297
250	0.401	0.474	0.602	0.0257	0.122	0.198	0.264
260	0.357	0.427	0.545	0.0229	0.110	0.178	0.238
270	0.326	0.387	0.496	0.0206	0.0984	0.161	0.215
280	0.296	0.352	0.452	0.0185	0.0895	0.147	0.196
290	0.269	0.323	0.413	0.0168	0.0809	0.133	0.179

TABLE V

SECONDARY TARGET TOTAL ATTENUATION COEFFICIENTS (μ_k)

k (keV)	Cu (cm^2/g)	Br (cm^2/g)	Mo (cm^2/g)	Ag (cm^2/g)	Ba (cm^2/g)	Gd (cm^2/g)	Yb (cm^2/g)
8.98	285						
13.47		149					
15	73.9	112	28.1	39.4	63.1	92.3	118
20.00	33.7	52.5	13.1	18.1	29.0	42.9	56.0
			82.2				
25.51				9.60			
				55.8			
30	10.8	17.4	28.0	36.6	9.73	14.6	19.1
37.44					5.48		
					29.1		
40	4.82	7.91	12.9	17.1	24.0	6.82	8.98
50	2.59	4.28	6.97	9.38	13.7		5.05
50.24						3.80	
						18.5	
60	1.58	2.41	4.25	5.75	7.54	11.2	
61.33							2.95
							13.5
70	1.07	1.70	2.86	3.88	5.70	7.81	9.74
76.11							
80	0.756	1.20	1.95	2.64	3.95	5.55	6.89
88.00							
90	0.573	0.889	1.43	1.93	2.89	4.06	5.05
100	0.453	0.684	1.09	1.46	2.18	3.08	3.83
109.65							
110	0.375	0.554	0.860	1.14	1.71	2.41	3.01
120	0.319	0.456	0.697	0.921	1.36	1.93	2.42
130	0.276	0.383	0.577	0.759	1.11	1.59	1.98
140	0.244	0.329	0.490	0.636	0.921	1.31	1.63
150	0.220	0.286	0.417	0.539	0.781	1.10	1.38
160	0.201	0.256	0.364	0.469	0.667	0.942	1.17
170	0.186	0.230	0.322	0.413	0.574	0.812	1.01
180	0.173	0.211	0.289	0.366	0.504	0.709	0.870
190	0.163	0.194	0.261	0.328	0.443	0.620	0.766
200	0.154	0.182	0.240	0.295	0.401	0.548	0.682
210	0.147	0.170	0.220	0.270	0.362	0.494	0.609
220	0.140	0.161	0.204	0.246	0.329	0.444	0.543
230	0.135	0.152	0.190	0.229	0.300	0.402	0.494
240	0.130	0.145	0.180	0.213	0.274	0.370	0.452
250	0.126	0.139	0.170	0.200	0.256	0.339	0.414
260	0.122	0.133	0.161	0.188	0.238	0.314	0.379
270	0.118	0.130	0.154	0.179	0.222	0.291	0.348
280	0.116	0.124	0.148	0.169	0.210	0.274	0.327
290	0.113	0.122	0.143	0.161	0.197	0.257	0.303

TABLE V (cont)

k (keV)	Ir (cm^2/g)	Pb (cm^2/g)	Th (cm^2/g)	NaBr (cm^2/g)	BaS (cm^2/g)	Gd_2O_3 (cm^2/g)	Yb_2O_3 (cm^2/g)
8.98							
13.47				117			
15	152			88.0	54.0	80.3	104
20.00	72.4	85.2		41.2	24.8	37.3	49.3
25.51							
30	25.2	29.9	38.4	13.7	8.28	12.7	16.8
37.44					4.66		
					23.8		
40	11.9	14.2	18.4	6.23	20.1	5.95	7.92
50	6.64	7.88	10.3	3.39	11.2		4.46
50.24						3.32	
						16.1	
60	4.17	4.94	6.49	1.92	7.70	10.2	2.77
61.3							2.61
							11.9
70	2.79	3.40	4.54	1.36	4.79	6.80	8.57
76.11	2.26						
	9.62						
80	8.49	2.37	3.11	0.972	3.25	4.84	6.07
88.0		1.88					
		7.56					
90	6.36	7.18	2.34	0.727	2.38	3.54	4.45
100	4.82	5.52	1.76	0.566	1.81	2.69	3.38
109.65			1.42				
			5.27				
110	3.79	4.30		0.464	1.42	2.11	2.66
120	3.07	3.49	4.20	0.387	1.14	1.69	2.14
130	2.51	2.86	3.45	0.329	0.923	1.40	1.76
140	2.07	2.38	2.88	0.286	0.776	1.15	1.45
150	1.74	2.01	2.47	0.252	0.662	0.972	1.23
160	1.47	1.69	2.08	0.228	0.568	0.835	1.04
170	1.27	1.46	1.80	0.207	0.492	0.722	0.903
180	1.10	1.28	1.56	0.192	0.434	0.632	0.780
190	0.971	1.09	1.38	0.178	0.384	0.555	0.688
200	0.858	0.994	1.22	0.168	0.350	0.492	0.614
210	0.768	0.890	1.09	0.159	0.317	0.445	0.550
220	0.689	0.799	0.976	0.151	0.290	0.401	0.491
230	0.627	0.721	0.882	0.144	0.266	0.364	0.448
240	0.570	0.660	0.802	0.138	0.245	0.336	0.411
250	0.517	0.602	0.727	0.133	0.230	0.309	0.377
260	0.476	0.549	0.667	0.128	0.215	0.287	0.347
270	0.439	0.503	0.615	0.125	0.201	0.267	0.319
280	0.407	0.471	0.568	0.120	0.191	0.252	0.301
290	0.376	0.430	0.527	0.118	0.181	0.237	0.279

$$dI_{coh} = (I_{primary}/r_r^2) \times (A_f/\sin\theta)\,(d\sigma_{coh}/d\Omega) \times \exp\{-\mu_k x/\sin\theta - \mu_k x/\cos\theta\} \times dx \quad (11)$$

Integration over the total thickness t of the target, with $\theta = 45°$, gives

$$I_{coh} = I_{primary}\,(A_f/r_r^2) \times \frac{d\sigma_{coh}/d\Omega}{2\mu_k} \times \left[1 - \exp\{-2\sqrt{2}\mu_k t\}\right], \quad (12)$$

where I_{coh} is in units of photons/s-mA-keV-sr.

The probability of coherent interaction is given by the Thomson scattering equation with corrections for electron binding

$$\frac{d\sigma_{coh}}{d\Omega} = \frac{r_o^2}{2}(1 + \cos\phi) \times \left[F_{q,Z}\right]^2 , \quad (13)$$

where r_o is the classical electron radium and ϕ is the scattering angle. The term $(r_o^2/2)(1 + \cos^2\phi)$ is the Thomson scattering cross section from one electron. F is a form factor representing the probability that the recoil momentum q is transferred to the Z electrons of an atom without energy absorption. We used Cromer's[19] form factors in this calculation. The $d\sigma_{coh}/d\Omega$ values for $\phi = 90°$ are given in Table VI for the targets used.

E. Incoherently Scattered Photons

In Compton or incoherent scatter, a photon with energy k interacts with the atomic electrons in the layer dx and is reradiated with lower energy k'. For 90° scatter

$$k' = \frac{k}{1 + (k/m_o c^2)} , \quad (14)$$

where $k/m_o c^2$ is the incident photon energy in electron rest-mass units. Solving Eq. (14) for k and differentiating gives the incident energy interval dk in terms of the scattered energy interval dk' so that

$$dk = \frac{dk'}{\{1 - (k'/m_o c^2)\}^2} . \quad (15)$$

Incoherently scattered photon intensities can be calculated from the third term in Eq. (6). The incoherent scattering coefficient σ_{inc}, which represents the probability of an incoherent interaction occurring summed over all angles of photon emission, must be replaced by $d\sigma_{inc}/d\Omega$, which represents the probability that a photon with energy k will interact incoherently in the layer dx and that a scattered photon with energy k' will emerge in the direction of the detector within the solid angle $d\Omega$.

In traveling from dx to the target surface, the scattered photon is attenuated by $\exp[-\mu_{k'} x/\cos\theta]$, where $\mu_{k'}$ is the total attenuation coefficient of the scattered photon with energy k'.

Thus the incoherently scattered photon intensity leaving the target in the direction of the detector from layer dx is

TABLE VI

SECONDARY TARGET COHERENT SCATTERING COEFFICIENTS
$(d\sigma_{coh}/d\Omega)$ FOR $\phi = 90°$

k (keV)	Cu (cm^2/g)	Br (cm^2/g)	Mo (cm^2/g)	Ag (cm^2/g)	Ba (cm^2/g)	Gd (cm^2/g)	Yb (cm^2/g)
15	0.0252	0.0372	0.0572	0.0659	0.0732	0.0877	0.101
20	0.0160	0.0192	0.0309	0.0406	0.0478	0.0540	0.0599
30	0.00821	0.00942	0.0113	0.0145	0.0225	0.0283	0.0308
40	0.00376	0.00550	0.00672	0.00743	0.00943	0.0145	0.0175
50	0.00177	0.00295	0.00433	0.00490	0.00557	0.00739	0.00933
61.20	0.000948	0.00145	0.00242	0.00307	0.00355	0.00414	0.00480
69.52	0.000687	0.000957	0.00160	0.00212	0.00272	0.00318	0.00355
80	0.000523	0.000632	0.000960	0.00132	0.00194	0.00239	0.00263
90	0.000417	0.000482	0.000672	0.000893	0.00135	0.00178	0.00202
100	0.000346	0.000392	0.000487	0.000614	0.000934	0.00133	0.00158
110	0.000281	0.000330	0.000389	0.000453	0.000627	0.000935	0.00120
120	0.000229	0.000284	0.000330	0.000375	0.000487	0.000705	0.000912
130	0.000174	0.000237	0.000286	0.000314	0.000392	0.000548	0.000651
140	0.000136	0.000196	0.000239	0.000268	0.000317	0.000429	0.000487
150	0.000108	0.000164	0.000211	0.000231	0.000267	0.000356	0.000393
160	0.0000849	0.000134	0.000182	0.000209	0.000234	0.000294	0.000328
170	0.0000645	0.000111	0.000159	0.000181	0.000204	0.000248	0.000275
180	0.0000488	0.0000904	0.000136	0.000160	0.000181	0.000208	0.000237
190	0.0000384	0.0000754	0.000117	0.000142	0.000161	0.000186	0.000216
200	0.0000301	0.0000633	0.000102	0.000125	0.000144	0.000168	0.000196
210	0.0000240	0.0000516	0.0000854	0.000110	0.000129	0.000152	0.000176
220	0.0000187	0.0000432	0.0000728	0.0000949	0.000117	0.000142	0.000161
230	0.0000152	0.0000353	0.0000615	0.0000837	0.000105	0.000129	0.000144
240	0.0000122	0.0000288	0.0000527	0.0000731	0.0000938	0.000115	0.000133
250	0.00000948	0.0000231	0.0000443	0.0000631	0.0000851	0.000108	0.000120
260	0.00000791	0.0000187	0.0000369	0.0000543	0.0000759	0.0000973	0.000112
270	0.00000616	0.0000151	0.0000304	0.0000463	0.0000688	0.0000885	0.000101
280	0.00000498	0.0000116	0.0000247	0.0000391	0.0000605	0.0000789	0.0000919
290	0.00000415	0.00000972	0.0000210	0.0000320	0.0000544	0.0000724	0.0000863

TABLE VI (cont)

k (keV)	Ir (cm^2/g)	Pb (cm^2/g)	Th (cm^2/g)	NaBr (cm^2/g)	BaS (cm^2/g)	Gd_2O_3 (cm^2/g)	Yb_2O_3 (cm^2/g)
15	0.122			0.0299	0.0621	0.0765	0.0891
20	0.0717	0.0823		0.0155	0.0400	0.0471	0.0529
30	0.0332	0.0355	0.0423	0.00764	0.0186	0.0247	0.0272
40	0.0204	0.0217	0.0234	0.00446	0.00770	0.0126	0.0154
50	0.0119	0.0136	0.0156	0.00239	0.00467	0.00643	0.00821
61.20	0.00598	0.00689	0.00919	0.00117	0.00298	0.00360	0.00422
69.52	0.00407	0.00451	0.00571	0.000768	0.00228	0.00276	0.00312
80	0.00291	0.00317	0.00381	0.000504	0.00162	0.00208	0.00231
90	0.00227	0.00253	0.00267	0.000381	0.00112	0.00155	0.00177
100	0.00181	0.00193	0.00211	0.000308	0.000775	0.00115	0.00139
110	0.00142	0.00157	0.00171	0.000258	0.000520	0.000811	0.00105
120	0.00112	0.00126	0.00143	0.000222	0.000402	0.000612	0.000801
130	0.000840	0.00100	0.00116	0.000185	0.000322	0.000475	0.000572
140	0.000617	0.000779	0.000945	0.000152	0.000260	0.000372	0.000428
150	0.000498	0.000631	0.000773	0.000127	0.000218	0.000309	0.000346
160	0.000404	0.000500	0.000618	0.000104	0.000190	0.000255	0.000288
170	0.000329	0.000398	0.000477	0.0000862	0.000165	0.000215	0.000242
180	0.000280	0.000334	0.000392	0.0000702	0.000147	0.000180	0.000208
190	0.000251	0.000291	0.000324	0.0000586	0.000131	0.000161	0.000190
200	0.000223	0.000249	0.000272	0.0000492	0.000116	0.000146	0.000172
210	0.000199	0.000222	0.000231	0.0000401	0.000105	0.000132	0.000155
220	0.000179	0.000195	0.000205	0.0000335	0.0000949	0.000123	0.000141
230	0.000160	0.000174	0.000179	0.0000274	0.0000851	0.000112	0.000126
240	0.000145	0.000158	0.000161	0.0000224	0.0000760	0.0000998	0.000117
250	0.000132	0.000144	0.000145	0.0000179	0.0000690	0.0000937	0.000105
260	0.000122	0.000132	0.000136	0.0000145	0.0000615	0.0000844	0.0000984
270	0.000110	0.000120	0.000123	0.0000117	0.0000558	0.0000768	0.0000887
280	0.0000996	0.000110	0.000114	0.00000901	0.0000490	0.0000685	0.0000807
290	0.0000921	0.000102	0.000105	0.00000755	0.0000441	0.0000678	0.0000758

$$dI_{inc} = (I_{primary}/r_r^2) \times (A_f/\sin\theta)\,(d\sigma_{inc}/d\Omega) \times \frac{1}{\{1 - (k'/m_oc^2)\}^2} \times \exp\{-\mu_k x/\sin\theta - \mu_{k'} x/\cos\theta\} \times dx \,. \quad (16)$$

The term $1/(1 - k'/m_oc^2)^2$ corrects for the change in the incident energy interval to the corresponding scattered energy interval and is obtained from Eq. (15). Integration of Eq. (16) over the total target thickness t with $\theta = 45°$ gives

$$I_{inc} = I_{primary}\,(A_f/r_r^2) \times \frac{1}{\{1 - (k'/m_oc^2)\}^2} \times \frac{d\sigma_{inc}/d\Omega}{\mu_k + \mu_{k'}} \times \left[1 - \exp\{-\sqrt{2}(\mu_k + \mu_{k'})t\}\right], \quad (17)$$

where I_{inc} is in units of photons/s-mA-keV-sr.

The cross section for photons interacting incoherently is given by the Klein-Nishina equation with corrections for electron binding

$$\frac{d\sigma_{inc}}{d\Omega} = \frac{Zr_o^2}{2}\left[1 + \alpha_o(1 - \cos\phi)\right]^{-2} \times \left\{1 + \cos^2\phi + \alpha_o^2(1-\cos\phi)^2 \times \left[1 + \alpha_o(1 - \cos\phi)\right]^{-1}\right\} \times S_{q,Z} \,, \quad (18)$$

where $\alpha_o = k/m_oc^2$, the incident photon energy. The differential form of the Klein-Nishina equation gives the cross section for photon deflection at a given angle ϕ and transfer of momentum to the electron as though it were free. S is the incoherent scattering function or probability that an atom will rise to an excited or ionized state when the photon imparts a recoil momentum q to any of the atomic electrons. Incoherent scattering functions used in the calculation were those of Cromer and Mann[20] and Cromer.[21] Values of $d\sigma_{inc}/d\Omega$ for $\phi = 90°$ are given in Table VII for the targets used. Table VIII gives the total attenuation coefficients $\mu_{k'}$ of the scattered photons.[22] The coherently scattered K edge and incoherently scattered K'-edge energies are listed in Table III for the secondary targets, together with the tungsten coherently and incoherently scattered K-edge and K-line energies.

F. Total Photons at the Detector

The solid angle subtended at the detector is A_d/r_d^2, where A_d is the detector aperture area and r_d is the distance from the fluorescent diaphragm to the detector aperture. Thus, the total photon intensity incident on the detector is

TABLE VII

SECONDARY TARGET INCOHERENT SCATTERING COEFFICIENTS
$(d\sigma_{inc}/d\Omega)$ FOR $\phi = 90°$

k' (keV)	k (keV)	Cu (cm^2/g)	Br (cm^2/g)	Mo (cm^2/g)	Ag (cm^2/g)	Ba (cm^2/g)	Gd (cm^2/g)	Yb (cm^2/g)
15	15.5	0.00678	0.00580	0.00571	0.00553	0.00509	0.00467	0.00438
20	20.8	0.00744	0.00663	0.00640	0.00625	0.00561	0.00529	0.00505
30	32.0	0.00815	0.00761	0.00728	0.00703	0.00645	0.00624	0.00602
40	43.3	0.00834	0.00784	0.00760	0.00737	0.00675	0.00663	0.00651
50	55.2	0.00834	0.00784	0.00772	0.00760	0.00688	0.00674	0.00665
61.2	69.5	0.00815	0.00769	0.00766	0.00754	0.00688	0.00678	0.00668
69.5	80.5	0.00796	0.00754	0.00753	0.00748	0.00684	0.00678	0.00661
80	95.0	0.00767	0.00739	0.00734	0.00726	0.00680	0.00659	0.00654
90	109	0.00749	0.00720	0.00716	0.00709	0.00667	0.00651	0.00637
100	125	0.00720	0.00701	0.00697	0.00690	0.00658	0.00636	0.00630
110	140	0.00706	0.00678	0.00684	0.00670	0.00645	0.00624	0.00623
120	157	0.00682	0.00659	0.00659	0.00653	0.00623	0.00613	0.00602
130	174	0.00663	0.00637	0.00634	0.00631	0.00592	0.00586	0.00581
140	193	0.00635	0.00614	0.00612	0.00609	0.00566	0.00571	0.00560
150	213	0.00611	0.00588	0.00590	0.00581	0.00544	0.00544	0.00536
160	233	0.00588	0.00565	0.00565	0.00562	0.00526	0.00529	0.00522
170	255	0.00569	0.00543	0.00552	0.00547	0.00504	0.00506	0.00508
180	278	0.00545	0.00524	0.00527	0.00525	0.00487	0.00490	0.00487
189	300	0.00527	0.00505	0.00506	0.00504	0.00474	0.00471	0.00466

TABLE VII (cont)

k' (keV)	k (keV)	Ir (cm^2/g)	Pb (cm^2/g)	Th (cm^2/g)	NaBr (cm^2/g)	BaS (cm^2/g)	Gd_2O_3 (cm^2/g)	Yb_2O_3 (cm^2/g)
15	15.5	0.00407			0.00648	0.00571	0.00530	0.00500
20	20.8	0.00479	0.00468		0.00719	0.00625	0.00589	0.00563
30	32.0	0.00570	0.00558	0.00532	0.00802	0.00703	0.00676	0.00653
40	43.3	0.00623	0.00610	0.00579	0.00820	0.00728	0.00708	0.00694
50	55.2	0.00639	0.00637	0.00607	0.00816	0.00737	0.00717	0.00703
61.2	69.5	0.00655	0.00640	0.00623	0.00797	0.00732	0.00713	0.00701
69.5	80.5	0.00655	0.00640	0.00623	0.00780	0.00725	0.00709	0.00691
80	95.0	0.00636	0.00634	0.00618	0.00761	0.00716	0.00686	0.00680
90	109	0.00630	0.00625	0.00610	0.00740	0.00700	0.00674	0.00660
100	125	0.00627	0.00616	0.00602	0.00718	0.00686	0.00658	0.00651
110	140	0.00623	0.00610	0.00597	0.00693	0.00670	0.00645	0.00642
120	157	0.00602	0.00599	0.00581	0.00672	0.00647	0.00631	0.00620
130	174	0.00580	0.00578	0.00563	0.00649	0.00617	0.00605	0.00599
140	193	0.00561	0.00555	0.00540	0.00626	0.00590	0.00588	0.00577
150	213	0.00536	0.00529	0.00519	0.00600	0.00568	0.00561	0.00552
160	233	0.00520	0.00515	0.00503	0.00578	0.00549	0.00545	0.00537
170	255	0.00498	0.00494	0.00485	0.00556	0.00527	0.00522	0.00523
180	278	0.00476	0.00477	0.00467	0.00535	0.00508	0.00504	0.00501
189	300	0.00464	0.00456	0.00449	0.00516	0.00493	0.00485	0.00479

TABLE VIII

SECONDARY TARGET TOTAL ATTENUATION COEFFICIENTS
FOR SCATTERED PHOTONS ($\mu_{k'}$)

k' (keV)	Cu (cm^2/g)	Br (cm^2/g)	Mo (cm^2/g)	Ag (cm^2/g)	Ba (cm^2/g)	Gd (cm^2/g)	Yb (cm^2/g)
15	89.1	105	25.9	47.2	57.9	84.3	108
19.25			13.1				
			82.2				
20	30.3	47.5	75.3	16.6	26.3	38.3	50.1
24.30				9.60			
				55.8			
30	9.10	14.7	23.6	31.0	8.33	12.4	16.2
34.88					5.48		
					29.1		
40	3.90	6.48	10.4	14.0	20.2	5.67	7.24
45.74						3.80	
						18.5	
50	1.50	3.24	5.24	7.03	10.7	14.3	3.83
54.76							2.95
							13.5
61.20	1.07	1.70	2.86	3.88	5.79	7.93	9.57
66.24							
69.52	0.741	1.18	1.91	2.64	3.90	5.48	6.79
75.07							
80	0.512	0.776	1.87	1.67	2.52	3.15	4.45
90.28	0.379	0.565	0.879	1.17	1.75	2.45	3.06
100	0.294	0.418	0.634	0.837	1.23	1.75	2.18
110	0.244	0.328	0.489	0.642	0.921	1.31	1.64
120	0.206	0.264	0.380	0.491	0.702	0.996	1.24
130	0.180	0.222	0.311	0.394	0.548	0.766	0.957
140	0.161	0.188	0.254	0.318	0.434	0.594	0.741
150	0.145	0.166	0.213	0.262	0.351	0.475	0.592
160	0.134	0.149	0.188	0.223	0.292	0.394	0.480
170	0.124	0.136	0.166	0.195	0.247	0.326	0.393
180	0.116	0.126	0.149	0.170	0.213	0.276	0.320
189	0.111	0.118	0.137	0.155	0.189	0.241	0.285

TABLE VIII (cont)

k' (keV)	Ir (cm^2/g)	Pb (cm^2/g)	Th (cm^2/g)	NaBr (cm^2/g)	BaS (cm^2/g)	Gd_2O_3 (cm^2/g)	Yb_2O_3 (cm^2/g)
15	139			84.5	49.6	73.3	95.0
19.25							
20	65.8	77.9		37.3	22.4	33.3	44.1
24.30							
30	21.5	25.6	32.7	11.6	7.08	10.8	14.3
34.88					4.66		
					23.8		
40	9.87	11.6	15.1	5.11	16.5	4.95	6.39
45.74						3.32	
						16.1	
50	5.23	5.96	7.91	2.57	8.76	12.4	3.39
54.76							2.61
							11.9
61.20	2.82	3.40	4.54	1.36	4.75	6.90	8.43
66.24	2.26						
	9.62						
69.52	8.30	2.36	3.09	0.956	3.21	4.78	5.99
75.07		1.88					
		7.56					
80	5.55	6.34	2.04	0.639	2.08	3.06	3.93
90.28	3.92	4.74	1.42	0.473	1.45	2.15	
			5.27				
100	2.76	3.14	3.81	0.357	1.03	1.54	1.93
110	2.07	2.37	2.88	0.285	0.776	1.15	1.46
120	1.54	1.79	2.18	0.235	0.597	0.882	1.11
130	1.21	1.38	1.70	0.201	0.470	0.682	0.856
140	0.934	1.08	1.32	0.173	0.377	0.532	0.666
150	0.736	0.860	1.06	0.155	0.308	0.428	0.535
160	0.605	0.701	0.856	0.141	0.259	0.357	0.436
170	0.498	0.576	0.698	0.130	0.222	0.298	0.359
180	0.414	0.477	0.571	0.122	0.194	0.254	0.294
189	0.351	0.398	0.485	0.115	0.174	0.223	0.263

$$I_{detector} = (A_d/r_d^2) \times \left[I_{K_\alpha} + I_{K_\beta} + I_{coh} + I_{inc}\right] \times \exp\left[-(\mu t)_{Al} - \Sigma(\mu t)_{det}\right], \quad (19)$$

where μ is the appropriate total attenuation coefficient for the fluorescent and scattered photon energy. The exponentials correct for the aluminum L-line filter and the intervening Mylar, air, and detector window attenuation. I_{K_α}, I_{K_β}, I_{coh}, and I_{inc} are given by Eqs. (9), (10), (12), and (17), respectively.

IV. COMPARISON OF MEASUREMENT AND THEORY

A. Undistorted Scattered Spectra

Typical undistorted scattered spectra calculated for secondary targets of Z = 42, 64, and 82 are shown in Fig. 16 for a 250-kV potential. The coherent continuum calculated from Eq. (12), the incoherent continuum calculated from Eq. (17), the total continuum, and the tungsten K lines are shown, but the fluorescent K lines excited in the secondary targets have been omitted. There are four K edges and four K lines. The coherently scattered primary and secondary K edges and the primary K_α and K_β lines appear, as well as the incoherently scattered primary and secondary K' edges and the primary K_α' and K_β' lines. The location of the tungsten K edges and K lines, together with the secondary K edges, are listed in Table III.

For purposes of discussion, the scattered spectra in Fig. 16 may be divided into three energy regions: a lower region k < K lines, a middle region K lines <k < k'_0, and an upper region k > k'_0. In the lower region, the coherent and incoherent interactions contribute to the intensity, with the former tending to

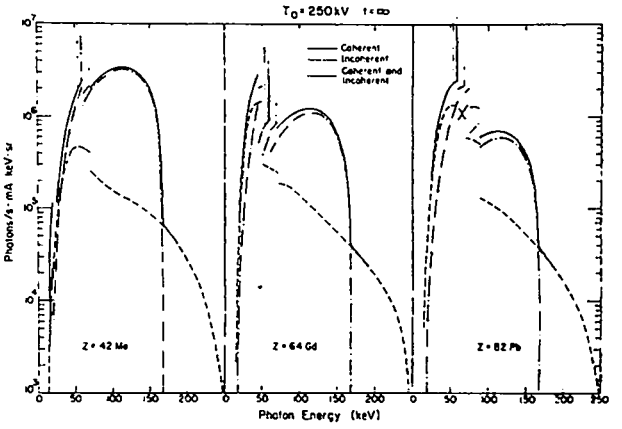

Fig. 16.
Calculated coherent and incoherent spectra for Z=42, 64, and 82. Secondary K lines are not included.

dominate. In the middle region, the incoherent interaction is responsible for most of the scattered intensity. In the upper region, only coherent scattering occurs. Thus, the calculated total 90° scattered spectra possess the complicated structured shape shown in Fig. 16. The incoherent cutoff energy k'_0 given by Eq. (14) varies with operating potential, having values of 84, 116, 144, 168, and 189 keV for potentials of 100, 150, 200, 250, and 300 kV, respectively.

B. Comparison of Spectral Distributions

The spectral distribution at the detector is given by Eq. (19). As with the primary beam, the spectra are distorted by the detectors, and the measurements show that each of the three detectors distorts the spectra differently. To compare theory with measurement, the calculated spectra were distorted using the Monte Carlo program developed by Israel.[16] As described above, the geometry and resolution of the detector are input data, and the program distorts the calculated spectrum so that it can be compared directly with measurement. Results are shown in Figs. 4-14, where the solid lines are the distorted calculated spectra. The structured shapes appearing in the calculated spectra of Fig. 16 are for the most part obscured by detector distortions.

Figure 4 gives the silicon detector results for Z = 29, 35, and 42 and potentials of 100, 200, and 300

keV. The measured and calculated K-photon intensities tend to agree, but the poor silicon detector efficiency causes the counting rate to be low and the measured points to scatter appreciably, making it difficult to compare the results of the 90° scattered spectra. Figures 5-8 give the germanium detector results for $42 \leq Z \leq 90$, and the measured and calculated K-photon intensities tend to agree. Counting rates are higher and measurements of the 90° scattered spectra are in better agreement with calculation; the points tend to scatter about the calculated line. The largest discrepancies occur at <20 keV, caused in part by large detector leakage currents. Figures 9-12 give the NaI detector results for $42 \leq Z \leq 90$, and the agreement is quite good. Again, poorest agreement occurs at <20 keV, where measured Compton scatter is larger than calculated. Figures 13 and 14 give the spectra obtained with three different target thicknesses instead of three different potentials. For a potential of 250 kV, copper, molybdenum, gadolinium, and lead spectra measured with the three different detectors are shown. For these measurements, metallic gadolinium was used instead of the oxide powder. Measured and calculated spectra show the same trend when the target thickness is varied. The discrepancies are similar to those described above and appear to be associated with the type of detector.

In summary, although there are regions where large discrepancies occur, particularly at <20 keV, the overall agreement between measured and calculated spectra is good and tends to be within 20%.

C. Comparison of Total Intensities

The total number of K_α plus K_β photons emitted from the target can be estimated from the spectrometer measurements by summing the total number of counts under the photo and escape peaks and subtracting the continuum. This procedure was applied to spectral measurements obtained at potentials of 100, 200, and 300 kV (Figs. 4-12) and to spectral measurements obtained at 150 and 250 kV (not shown). The total number of K photons emitted from the target, as estimated from the spectrometer measurements, with corrections for aluminum and detector filtration, is plotted as a function of primary potential T_0 in Fig. 17 for each of the 10 secondary

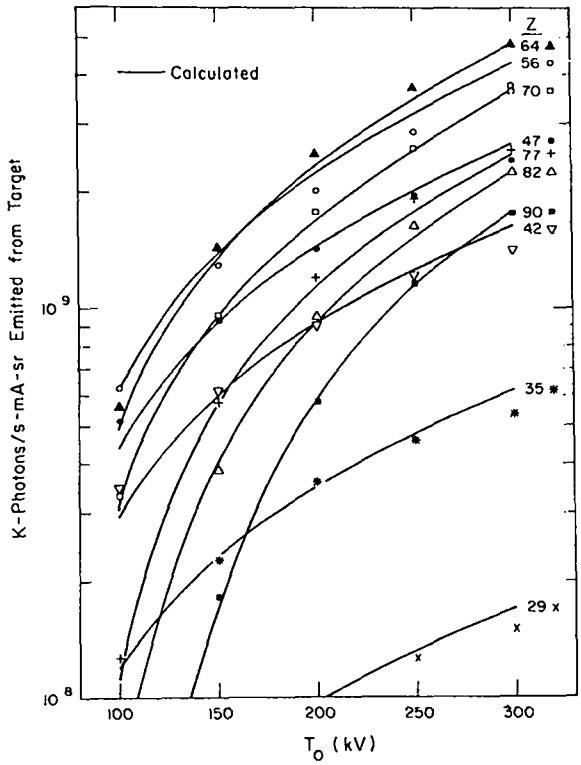

Fig. 17.
Calculated total intensity in photons compared to spectral measurements.

targets. The total K_α, K_β intensity was also calculated from Eqs. (9) and (10), and the results are given by the solid curves in Fig. 17. In all cases, the measured points are within 15% of the calculated curves.

As an additional check on the theory, the intensity from the targets was measured in roentgens with a free-air ionization chamber. In Fig. 18, the measured intensities 15 cm from the secondary target are plotted as a function of primary potential for each of the 10 secondary targets. The total calculated K_α, K_β, coherent, and incoherent photon intensity, with corrections for aluminum and air attenuation, is also given in Fig. 18 by the solid curves for a secondary target-to-detector distance of 15 cm. Because the free-air chamber measured the scattered radiation and the K-line radiation, the scattered contribution was included in the calculation. For the higher Z materials, the measured points tend to fall above the calculated curves at the higher potentials, but in all cases, the points are within 20% of the calculated curves.

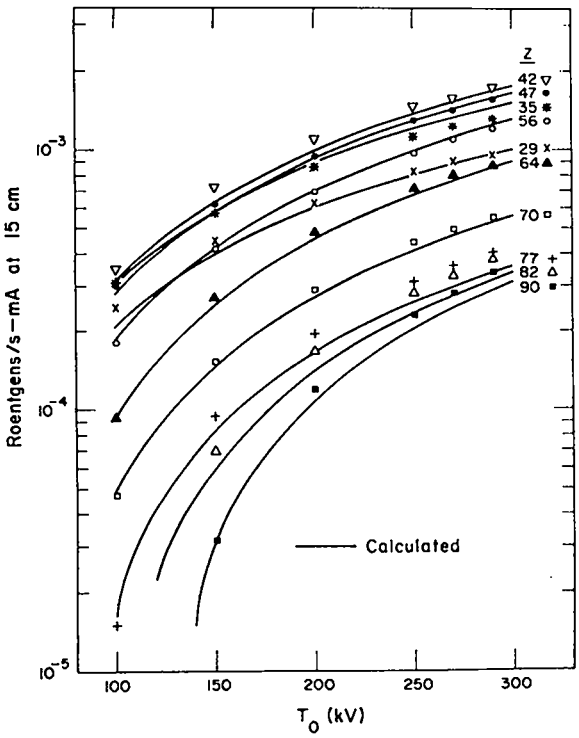

Fig. 18.
Calculated total intensity in roentgens compared with free-air chamber measurements.

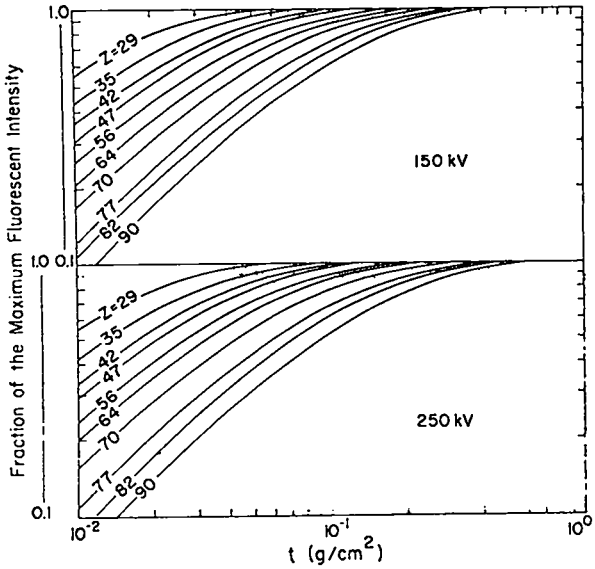

Fig. 19.
Fraction of the maximum attainable K-intensity as a function of target thickness. The ordinate is the ratio of K intensity at a given target thickness to that obtained with an infinitely thick target.

V. OPTIMIZATION OF K-PHOTON INTENSITY AND PURITY

A. Target Thickness

The target thickness appears in the $(1-e^{-\mu t})$ terms of the K-photon equations, Eqs. (9) and (10), and the scatter equations, Eqs. (12) and (17). The K photon and scatter intensities increase with thickness, approaching a maximum value exponentially. Because $1 - e^{-\mu t} = 1$ when $t = \infty$, maximum intensities are obtained with infinitely thick targets. Intensities were calculated for thicknesses in the range $0.01 \leq t \leq 10$ g/cm^2 and were compared with the intensities obtained with infinitely thick targets. Figure 19 gives the ratio of the K-photon intensity obtained with a finite target to the intensity obtained with an infinitely thick target as a function of target thickness for excitation potentials of 150 and 250 kV. The ratio represents the fraction of the maximum K-photon intensity attainable with a given target thickness with all other variables held constant. A similar plot giving the fraction of the maximum scattered intensity as a function of thickness is shown in Fig. 20. Because the dependence on Z is of interest here, these and all other calculations performed in the remainder of this report were for the 10 elemental targets only. Values of τ_k, μ_k, $d\sigma_{coh}/d\Omega$, $d\sigma_{inc}/d\Omega$, and $\mu_{k'}$ are given in Tables IV-VIII; μ_{K_α} and μ_{K_β} are listed in Table III.

The K-photon curves in Fig. 19 behave differently with atomic number than do the scatter curves in Fig. 20. For a given target thickness, the fraction of the maximum K-photon intensity is largest for the lowest Z and decreases as Z increases, whereas the fraction of the maximum scattered intensity is largest for the highest Z and decreases as Z decreases.

The K-photon behavior with Z is explained by considering that K-photon energies increase with Z, and attenuation coefficients are large at low energies, tending to decrease as energy increases. For example, the K_α energy for Z = 29 is 8 keV and $\mu_{K_\alpha} = 50.2$ (Table III), whereas the K_α energy for Z = 90 is 92 keV and $\mu_{K_\alpha} = 2.21$. Hence, the 8-keV photon is

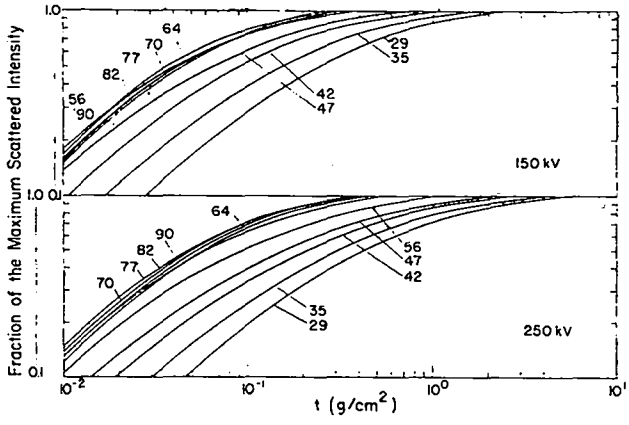

Fig. 20.
Fraction of the maximum attainable scattered intensity as a function of target thickness. The ordinate is the ratio of scattered intensity at a given target thickness to that obtained with an infinitely thick target.

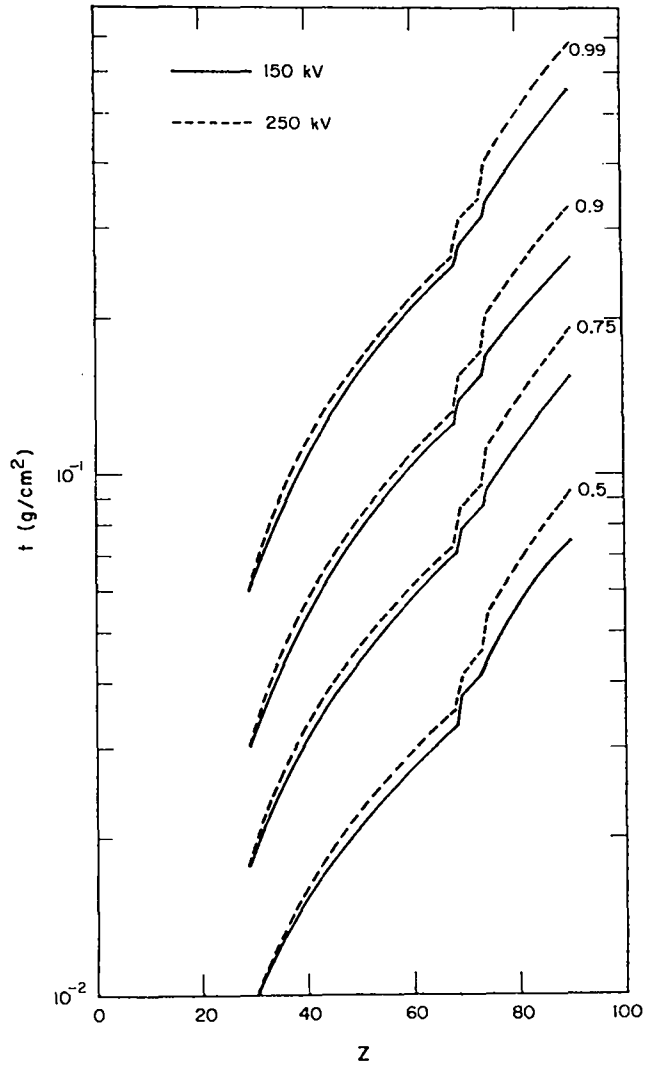

Fig. 21.
Target thicknesses required to obtain fractions of 0.5, 0.75, 0.9, and 0.99 of the maximum attainable K intensity.

strongly attenuated in leaving the target, and only those photons produced near the surface can escape. On the other hand, the 92-keV photons suffer far less attenuation and can escape from a much greater target depth. Thus, to obtain a given fraction of the maximum K-photon intensity, much thicker targets are required for Z = 90 than for Z = 29. This is shown in Fig. 21, where the thickness required to achieve fractions of 0.5, 0.75, 0.9, and 0.99 of the maximum attainable K-photon intensity are given as a function of Z for potentials of 150 and 250 kV. The curves increase rapidly with Z, but are weakly dependent on the primary potential. The discontinuities are caused by the tungsten K_α-(58.8 keV) and K_β-(67.6 keV) lines in the primary beam which can excite K photons only above the Z = 68 K edge (57.5 keV) and the Z = 73 K edge (67.4 keV), respectively.

The behavior of scattered radiation with Z is more difficult to explain. The scattered primary photon energy distribution is similar in each target. Tables V and VIII, which give μ_k and $\mu_{k'}$ as a function of energy, show that for a given energy the total attenuation coefficient tends to increase as Z increases. Hence, for the same target thicknesses, the scattered photons leaving the targets suffer greater attenuation in the higher Z materials. This trend is affected to some extent by the target K-edge discontinuities when they occur near the tungsten K-line and K-edge energies. As a result, the fraction of maximum scattered intensity curves are only weakly dependent on atomic numbers of Z > 60. This can be seen more clearly in Fig. 22, where the thicknesses required to obtain fractions of 0.25, 0.5, 0.75, 0.9, and 0.99 of the maximum attainable scattered intensity are given as a fraction of Z for potentials of 150 and 250 kV. The curves at first decrease rapidly with Z, but level off and remain relatively constant above Z = 60. Also, the scattered intensity is more strongly dependent on the potential than on the K-photon intensity.

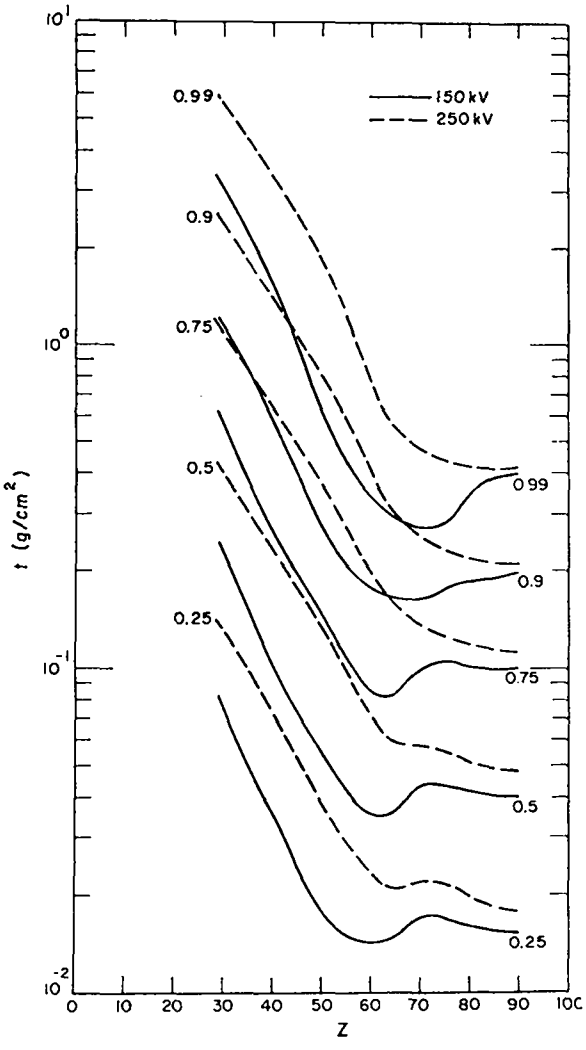

Fig. 22.
Target thicknesses required to obtain fractions of 0.25, 0.5, 0.75, 0.9, and 0.99 of the maximum attainable scattered intensity.

In most applications, target thicknesses are required that maximize either the K-photon intensity or the purity. Purity is plotted in Fig. 23 for the 10 elements as a function of target thickness for potentials of 150 and 250 kV. Over the thickness range studied, the purity of the low-Z targets (29, 35, 42) is highest at smallest thicknesses and decreases as thickness increases. Purity is relatively constant with thickness for Z = 47, 56, 64, and 70. For the high-Z targets (77, 82, 90), purity is lowest for the thinnest targets and increases as thickness increases, tending to level off at large thicknesses.

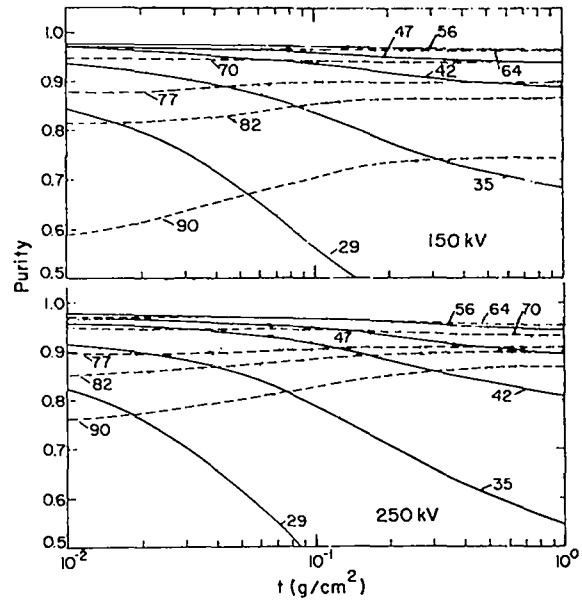

Fig. 23.
Purity as a function of target thickness.

The purity of those target thicknesses giving 0.5, 0.75, 0.9, and 0.99 of the maximum attainable K-photon intensity is shown in Fig. 24 as a function of Z for potentials of 150 and 250 kV. For $Z < 50$, purity decreases as the fraction of the maximum attainable K-photon intensity increases. For $Z > 50$, purity increases as the fraction increases. Hence, for $Z < 50$ one must choose between intensity and purity. For $Z > 50$, thicker targets give higher intensity and purity.

In summary, maximum K-photon intensity with the minimum scatter and maximum purity is obtained with target thicknesses labeled 0.99 in Fig. 21. Thicknesses larger than these will significantly increase the scatter but not the K-photon intensity. For $Z < 50$, purity can be improved by using thinner targets and sacrificing K-photon intensity. For example, at $Z = 29$ and $T_o = 250$ kV, a target thickness of 0.01 instead of 0.06 g/cm^2 increases the purity from 0.62 to 0.90, but decreases the K-photon intensity by one-half.

Target thicknesses labeled 0.99 in Fig. 21 for T_o = 250 kV were used in the remainder of the calculations discussed in this report.

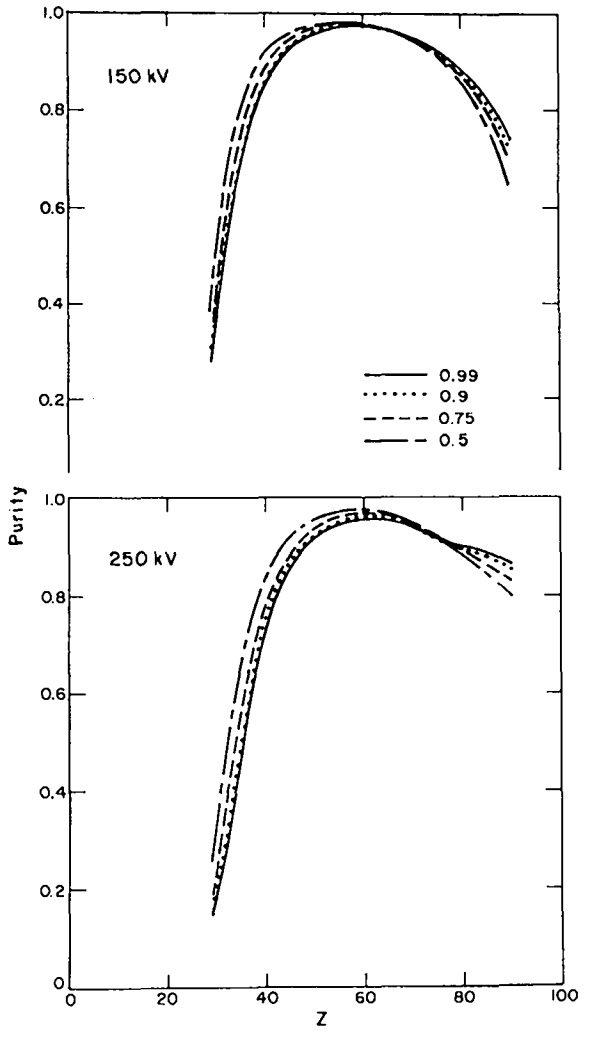

Fig. 24.
Purity as a function of Z for target thicknesses that give 0.5, 0.75, 0.9, and 0.99 of the maximum K intensity.

B. Primary Potential

The units in which an instrument is calibrated depend upon the intended application. In general, radiation laboratory instruments are calibrated in photons, x-ray astronomy and nuclear test detectors in ergs, and personnel dosimeters and health physics instruments in roentgens. Because the intensity of each unit is of interest, and purity varies with the unit of measurement, calculations were performed for each of these units.

The potential appears in the K photon and scatter equations in the $I_{primary}$ term, which represents the spectral distribution of the primary beam (Fig. 1). Total K-photon intensities were calculated from Eqs. (9) and (10), and total scattering intensities by summing Eqs. (12) and (17) over the photon energy range.

In Fig. 25, K-photon and scattered intensities are plotted in units of photons, ergs, and roentgens as a function of Z for each of the five potentials. The K-photon curves are strongly dependent on Z, varying in intensity by one to two orders of magnitude. The curves tend to be bell-shaped, with the intensity peaking near Z = 50-60. At higher potentials, the curves tend to rise in the upper Z region. The shape of the scatter curves is similar for a fixed potential, being relatively flat at low Z, rising between Z = 60-70 before leveling off again. Scatter varies by no more than a factor of 2 to 3 over the range $29 \leq Z \leq 90$.

Purity is plotted in Fig. 26 as a function of Z for the five potentials. Although purity is a dimensionless ratio, it varies with the intensity units. The photon curves peak at Z = 50-60 and decrease at low and high Z. Thus intensity and purity curves peak in the middle-Z region and fall off at both ends. Although similar trends are observed for ergs, purity is considerably less at low Z. For example, for Z = 29

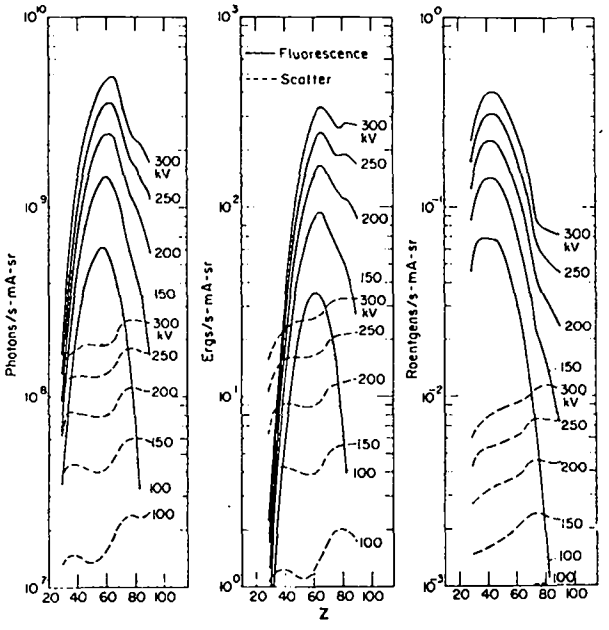

Fig. 25.
K and scatter intensity as a function of Z.

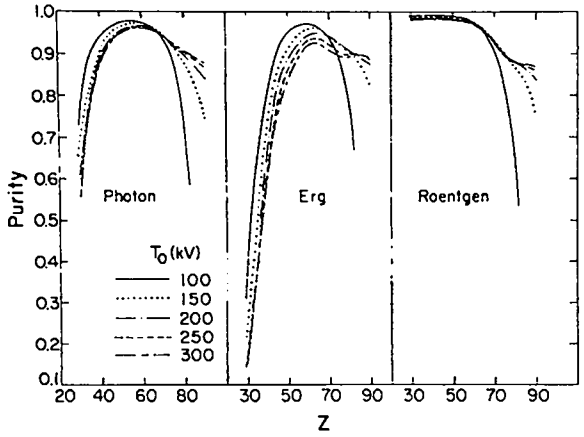

Fig. 26.
Purity as a function of Z.

and T_0 = 100 kV, purity is 0.73 in photons and only 0.34 in ergs. In roentgens, purity is relatively constant in the range $29 \leq Z \leq 64$, but decreases at higher Z.

Figure 27 shows intensity variation with potential for fixed Z, with K photon and scatter intensity in photons, ergs, and roentgens plotted as a function of T_0 for the 10 targets. The K photon and scatter intensity curves increase with increasing T_0, the rise being more rapid between 100 and 200 kV than between 200 and 300 kV. Evidently, the curves would continue to level off at still higher potentials. When the potential is increased from 100 to 300 kV, about a factor of 5 increase for $Z < 50$ and a factor of 10 increase for $Z > 50$ is obtained in the K-photon intensity, whereas an order of magnitude increase in scatter intensity is obtained at all Z.

It is evident from Fig. 27 that in the 100- to 300-kV potential range the x-ray tube should be operated at the highest potential to maximize K-photon intensity. However, because scatter also increases with potential, purity of the radiation must be considered. Purity is plotted in Fig. 28 in roentgens and photons and in Fig. 29 in ergs as a function of overvoltage $U_0 = T_0/T_K$, where T_K is the secondary target K-edge energy. For $U_0 < 1$, K-photon intensity and purity are zero. Because the photoelectric coefficient is a maximum at the upper K edge, for a given Z, the purity curve rises rapidly for $U_0 \geq 1$. In roentgens, purity increases, reaches a maximum near $U_0 = 3$, and remains relatively constant out to $U_0 = 30$. In photons, the curves reach a maximum in the range $3 < U_0 < 5$ and then decrease. In ergs,

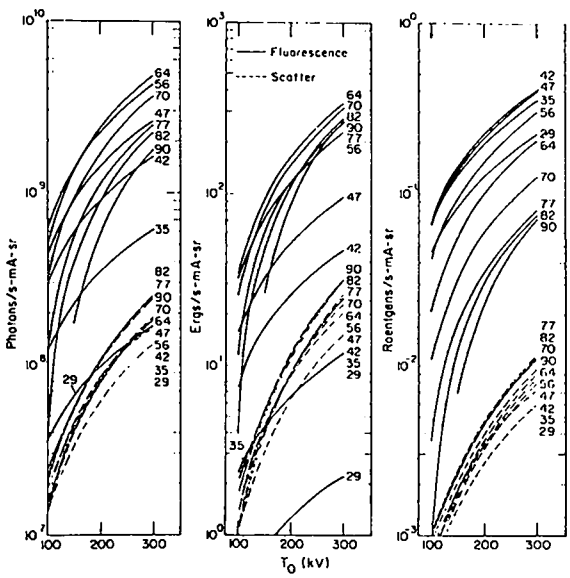

Fig. 27.
K- and scatter intensity as a function of potential.

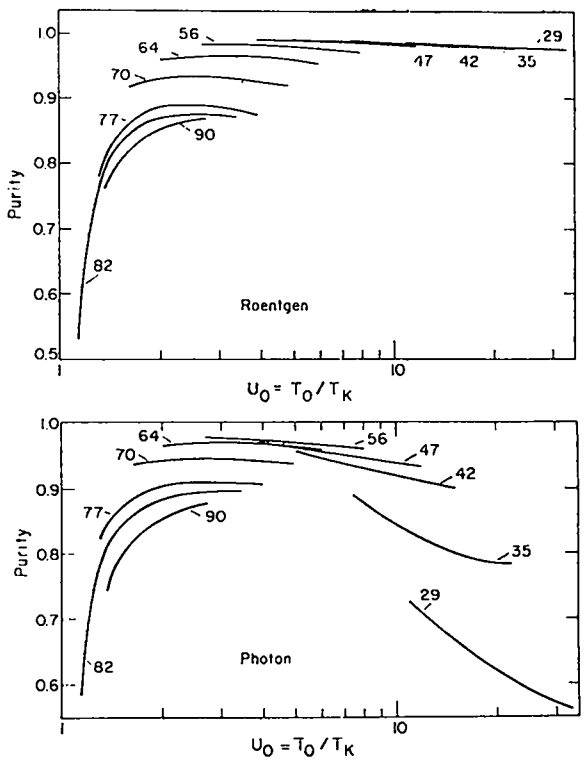

Fig. 28.
Purity in terms of roentgens and photons as a function of overvoltage.

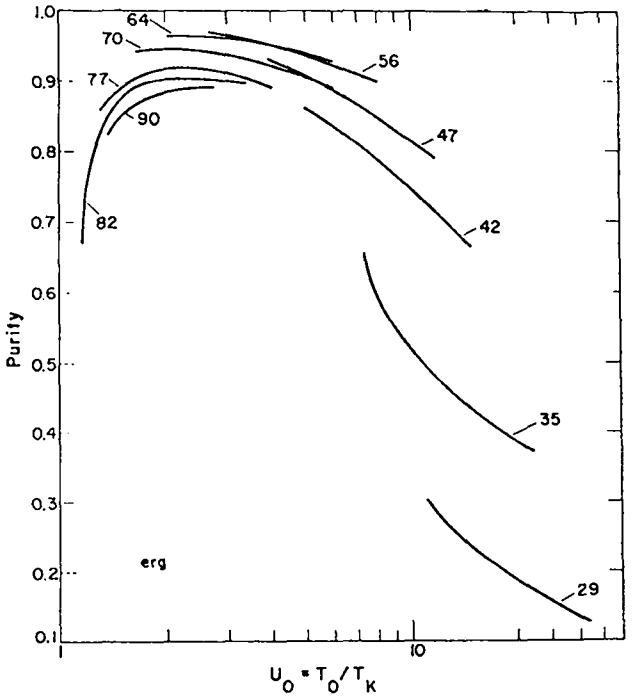

Fig. 29.
Purity in terms of ergs as a function of overvoltage.

maximum purity is reached more rapidly, but the region of constancy is in the narrower range $2 < U_o < 3$ and purity decreases more rapidly.

In summary, maximum K-photon intensity is obtained at maximum potential. In roentgens, maximum purity also occurs at the highest potential. Hence, a 300-kV potential will give maximum intensity and purity for all 10 targets. At 300 kV, purity is >0.95 for $29 \leq Z \leq 64$, but gradually decreases for higher Z, and reaches a low of 0.87 for Z = 90.

In photons, for Z = 29, purity improves from 0.56 at 300 kV to 0.73 at 100 kV. Similarly, for Z = 35, purity improves from 0.78 at 300 kV to 0.89 at 100 kV. If the K-photon intensity at 300 kV is taken as 1.0, the fraction obtained at 100, 150, 200, and 250 kV is about 0.16, 0.3, 0.5, and 0.75, respectively, for Z < 50. Hence, purity improvement for Z = 29 and 35 is achieved at the expense of a factor of 6 in intensity. For targets $42 \leq Z \leq 90$, purities of 0.88-0.96 are obtained at 300 kV.

In ergs, satisfactory purity for the lowest Z targets cannot be obtained even with low potentials. For example, with a 100-kV potential, purities of only 0.30 and 0.65 are obtained with Z = 29 and 35, respectively. As Z increases, purities improve so that higher potentials can be used. A 200-kV potential provides purities of 0.74 and 0.85 for Z = 42 and 47, respectively. With a 300-kV potential, purities of 0.89 to 0.93 are obtained for targets of $56 \leq Z \leq 90$.

C. K_β Filter

Table IX lists the K_α and K_β energies of the 10 targets. The K_α and K_β lines are separated by <4 keV and for Z < 50. However, the separation increases with Z and is 14 keV at Z = 90. A more monoenergetic source is required in calibration, if the instrument response is changing rapidly or K-edge structure is to be resolved. The K_β contribution can be reduced, with minimum reduction in the K_α-line, by using a filter with a K-edge energy between the K_α and K_β energies. A list of K_β filters which can be used with the 10 targets is given in Table IX. The table lists the K_β-filter atomic number, K-edge energy, and thickness that reduces the K_β-to-K_α ratio to 0.02. Also, the fraction of the K_α intensity transmitted by the K_β filter is given.

To demonstrate how the K_β filter alters the secondary target spectrum, calculated spectra are given for a low-Z (42) target in Fig. 30 and a high-Z (82) target in Fig. 31, with and without a K_β filter. With a Z = 42 target, the K_β filter (Z =41) reduces the K_β-to-K_α ratio to 0.02, decreases the K_α intensity to one-half, and has little effect on the scatter intensity. With a Z = 82 target, the K_β filter (Z = 78) reduces the K_β-to-K_α ratio to 0.02, decreases the K_α intensity to one-fourth, and appreciably reduces the scatter intensity.

K purity has been defined by the ratio $(I_{K_\alpha} + I_{K_\beta})/(I_{K_\alpha} + I_{K_\beta} + I_S)$, where I_{K_α}, I_{K_β}, and I_S are the K_α, K_β, and scatter intensities, respectively. If the K_β line is considered a contaminant, the K_α purity is defined by the ratio $(I_{K_\alpha})/(I_{K_\alpha} + I_{K_\beta} + I_S)$.

Tables X-XII list calculated values of I_{K_α}, I_{K_β}, I_S, K purity, and K_α purity in photons, ergs, and roentgens, respectively for the 10 secondary targets $29 \leq Z \leq 90$. Intensities were calculated for target thicknesses labeled 0.99 in Fig. 21.

In roentgens the scatter intensity I_S is so small that the reduction of the K_β line results in significant improvement in K_α purity for all 10 targets. In photons and ergs, however, the scatter intensity is

TABLE IX

SECONDARY TARGET K_β-FILTERS

Secondary Target Z	K_α-Energy (keV)	K_β-Energy (keV)	K_β-Filter (Z)	Filter K-Edge Energy (keV)	$K_\alpha/K_\beta = 0.02$ Filter (g/cm^2)	Transmitted K_α-Intensity
29	8.041	8.907	28	8.332	0.0085	0.663
35	11.907	13.300	34	12.658	0.022	0.544
42	17.443	19.648	41	18.986	0.037	0.519
47	22.103	25.008	45	23.220	0.060	0.478
56	32.062	36.535	53	33.170	0.12	0.422
64	42.750	48.918	60	43.569	0.21	0.367
70	52.014	59.652	66	53.788	0.30	0.315
77	64.303	73.919	72	65.345	0.46	0.271
82	74.159	85.370	78	78.395	0.54	0.268
90	92.050	106.169	84	93.105	0.84	0.217

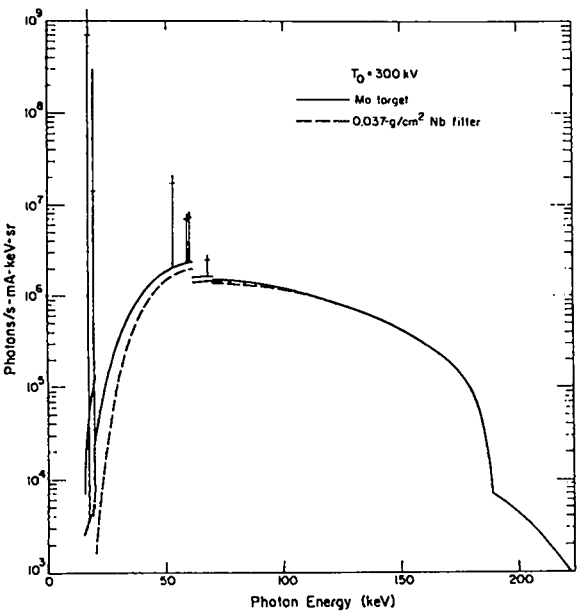

Fig. 30.

Calculated Z=42 secondary target spectrum with and without a Z=41 K_β filter. Molybdenum K_α (17.4 keV) and K_β (19.6 keV) lines are shown superimposed on 90° scattered spectrum. The coherently scattered molybdenum K edge (20 keV), tungsten K edge (69 keV), and tungsten K lines (59 and 68 keV) appear, as well as the incoherently scattered molybdenum K edge (19 keV), tungsten K edge (61 keV), and tungsten K lines (53 and 60 keV). Horizontal lines on line spectra indicate intensity peaks with K_β filter.

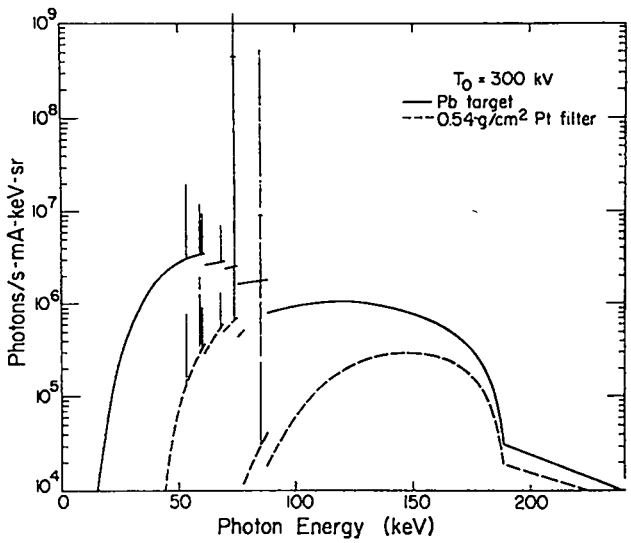

Fig. 31.

Calculated Z=82 secondary target spectrum with and without a Z=78 K_β filter. Lead K_α-(74 keV) and K_β (85 keV) lines are shown superimposed on 90° scattered spectrum. The coherently scattered lead K edge (88 keV), tungsten K edge (69 keV), and tungsten K lines (59 and 68 keV) appear, as well as the incoherently scattered lead K edge (75 keV), tungsten K edge (61 keV), and tungsten K lines (53 and 60 keV). Horizontal lines on line spectra indicate intensity peaks with K_β filter.

TABLE X

INTENSITY (photons/s-mA-sr) AND PURITY
OF SECONDARY TARGETS WITH AND WITHOUT K_β-FILTER

Target Z	Target Thickness (g/cm^2)	T_o (kV)	I_{K_α}	I_{K_β}	I_S	$\frac{I_{K_\alpha} + I_{K_\beta}}{I_T}$[a]	$\frac{I_{K_\alpha}}{I_T}$[a]	With K_β-Filter		
								I_{K_α}	I_S	$\frac{I_{K_\alpha}}{I_T}$[a]
29	0.06	100	3.06×10^8	4.67×10^7	1.33×10^7	0.726	0.630	2.03×10^7	1.29×10^7	0.604
35	0.09	100	1.02×10^9	1.86×10^8	1.50×10^8	0.889	0.752	5.55×10^8	1.34×10^8	0.792
42	0.12	300	1.33×10^9	2.96×10^8	1.84×10^8	0.898	0.735	6.90×10^8	1.60×10^8	0.798
47	0.15	300	2.12×10^9	5.05×10^8	1.88×10^8	0.933	0.754	1.01×10^9	1.49×10^8	0.856
56	0.20	300	3.41×10^9	8.84×10^8	1.85×10^8	0.959	0.761	1.44×10^9	1.10×10^7	0.911
64	0.25	300	3.76×10^9	1.03×10^9	1.97×10^8	0.960	0.754	1.38×10^8	7.81×10^7	0.929
70	0.32	300	2.86×10^9	7.95×10^8	2.46×10^8	0.937	0.733	9.01×10^8	6.96×10^7	0.911
77	0.47	300	1.90×10^9	5.78×10^8	2.58×10^8	0.906	0.693	5.15×10^8	4.67×10^7	0.900
82	0.53	300	1.70×10^9	5.32×10^8	2.56×10^8	0.898	0.683	4.55×10^8	3.43×10^7	0.913
90	0.67	300	1.34×10^9	4.32×10^8	2.48×10^8	0.876	0.663	2.91×10^8	1.49×10^7	0.933

[a] $I_T = I_{K_\alpha} + I_{K_\beta} + I_{K_S}$.

TABLE XI

INTENSITY (ergs/s-mA-sr) AND PURITY OF SECONDARY TARGETS WITH AND WITHOUT K_β-FILTER

Target Z	Target Thickness (g/cm^2)	T_o (kV)	I_{K_α}	I_{K_β}	I_S	$\frac{I_{K_\alpha} + I_{K_\beta}}{I_T}$[a]	$\frac{I_{K_\alpha}}{I_T}$[a]	With K_β-Filter: I_{K_α}	With K_β-Filter: I_S	With K_β-Filter: $\frac{I_{K_\alpha}}{I_T}$[a]
29	0.06	100	0.395	0.0663	1.05	0.305	0.261	0.261	1.02	0.203
35	0.09	100	1.94	0.396	1.23	0.655	0.544	1.06	1.12	0.481
42	0.12	200	20.6	5.11	8.95	0.742	0.594	10.7	7.90	0.568
47	0.15	200	41.0	10.7	9.20	0.849	0.673	19.6	7.43	0.713
56	0.20	300	175	51.6	25.5	0.899	0.694	73.9	18.0	0.789
64	0.25	300	257	78.9	26.4	0.927	0.709	94.4	13.8	0.856
70	0.32	300	238	75.9	31.0	0.910	0.690	75.0	11.8	0.847
77	0.47	300	194	68.2	32.7	0.889	0.658	52.8	8.07	0.851
82	0.53	300	201	72.9	33.0	0.892	0.655	53.8	6.07	0.880
90	0.67	300	197	73.4	33.0	0.891	0.649	42.8	2.79	0.918

[a] $I_T = I_{K_\alpha} + I_{K_\beta} + I_{K_S}$.

TABLE XII

INTENSITY (R/s-mA-sr) AND PURITY OF SECONDARY TARGETS WITH AND WITHOUT K_β-FILTER

Target Z	Target Thickness (g/cm^2)	T_o (kV)	I_{K_α}	I_{K_β}	I_S	$\frac{I_{K_\alpha} + I_{K_\beta}}{I_T}$[a]	$\frac{I_{K_\alpha}}{I_T}$[a]	With K_β-Filter I_{K_α}	With K_β-Filter I_S	With K_β-Filter $\frac{I_{K_\alpha}}{I_T}$[a]
29	0.06	100	0.0411	0.00508	0.000625	0.987	0.878	0.0271	0.000594	0.962
35	0.09	100	0.0598	0.00867	0.000653	0.991	0.865	0.0325	0.000561	0.967
42	0.12	300	0.346	0.0596	0.00793	0.981	0.837	0.179	0.00684	0.949
47	0.15	300	0.334	0.0596	0.00847	0.979	0.831	0.159	0.00664	0.945
56	0.20	300	0.247	0.0503	0.00897	0.971	0.806	0.104	0.00538	0.936
64	0.25	300	0.166	0.0382	0.00958	0.955	0.776	0.0612	0.00414	0.922
70	0.32	300	0.102	0.0260	0.0112	0.921	0.734	0.0322	0.00360	0.885
77	0.47	300	0.0613	0.0192	0.0114	0.876	0.667	0.0167	0.00243	0.858
82	0.53	300	0.0567	0.0194	0.0112	0.872	0.649	0.0152	0.00178	0.878
90	0.67	300	0.0520	0.0195	0.0109	0.868	0.631	0.0113	0.000792	0.914

[a] $I_T = I_{K_\alpha} + I_{K_\beta} + I_{K_S}$.

large. For low-Z targets, the K_β filter does not significantly reduce the scatter intensity (Fig. 30), and K_α purity is actually poorer with the K_β filter because of the K_α-line attenuation. For high-Z targets, the K_β filter reduces the scatter intensity (Fig. 31), and K_α purity is improved by the K_β filter.

When monochromaticity of the K lines is not important, the K_β filter need not be used, because K purity is better than K_α purity for all targets except Z=82 and 90. The small improvement in purity of these targets is achieved at the expense of K_α intensity, which is reduced by about a factor of 4.

D. Discussion

Because theory and measurement agreed within 20%, it was assumed that theory could be used to estimate target thicknesses, potentials, and K_β filters which would optimize K-photon intensity and purity. Tables X-XII summarize these estimates.

The intensity and purity of the lowest and highest Z targets leave something to be desired. Limitations on the achievable intensity and purity were imposed by the primary source used in the measurements and were assumed in the calculations. This can be seen more clearly in Fig. 32, where conversion efficiency in photons, ergs, and roentgens is plotted as a function of Z for five potentials in the 100- to 300-kV range. Conversion efficiency is defined as the ratio of K-photon intensity emitted by the secondary target to the primary photon intensity incident on the target. As with purity, the efficiency depends on the intensity units being most efficient for roentgens and least efficient for ergs. Maximum efficiencies of 2, 3, and 7% are obtained for the middle-Z targets in ergs, photons, and roentgens, respectively. Efficiency decreases for both low- and high-Z targets.

It is informative to inquire into the bell-shaped appearance of the conversion efficiency curves. If we examine Eq. (9), which describes the K_α intensity, the principal terms of interest are ω_K, $I_{primary}$, and $\tau \equiv \tau_k/(\mu_k + \mu_{K_\alpha})$. The exponential term and its influence on intensity and purity were discussed in Sec. V.A. The σ_K/σ_T term is approximately 0.8 for all Z. The fluorescent yield, ω_K, is >0.9 and roughly constant for $Z \geq 56$ but decreases at lower Z to a low of 0.455 for Z = 29. Hence, the decrease in efficiency for Z < 50 can be attributed in part to the decrease in ω_K with lower Z.

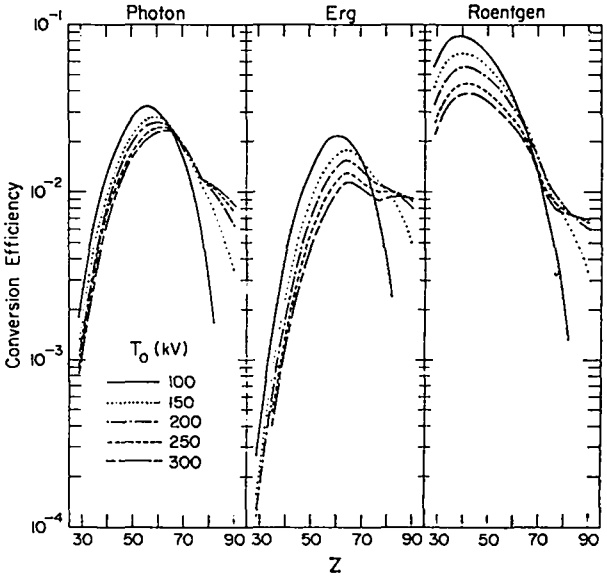

Fig. 32.
Conversion efficiency as a function of Z. The ordinate is the ratio of K intensity emitted by target-to-primary intensity incident on target.

But the shape of the efficiency curves is influenced primarily by τ, $I_{primary}$, and the location of the target K edge. For example, τ for Z = 29 is about 0.8 at the 9-keV K edge, but falls to 0.08 at 40 keV and to 0.008 at 90 keV. Because there are relatively few photons below 40 keV in $I_{primary}$, the K-photon yield is low for Z = 29. This implies that the yield can be increased by using a primary beam with more photons in the 9- to 40-keV region, e.g., one operating at a potential of 50 kV. For Z = 42, τ is 0.8 at the 20-keV K edge and falls to 0.08 at 80 keV. Because there are more primary photons in the 20- to 80-keV region than in the 9- to 40-keV region, the Z = 42 photon yield is considerably larger than the Z = 29 yield. Thus, as Z increases, τ remains significant over a longer photon region and the K-photon efficiency increases. For Z = 64, τ = 0.8 at the 50-keV K edge and 0.08 at 180 keV, giving a maximum yield for the $I_{primary}$ used in these calculations. As Z is increased further, τ remains significant over a longer photon region, but the K-edge location is increasing with energy, reducing the number of usable primary photons. For Z = 90, τ is 0.8 at the 110-keV K edge and decreases to 0.1 at 290 keV. But only photons above the K edge can produce K photons, so that all the primary photons below 110 keV are lost. Thus, the efficiency decreases. To improve the high-Z efficiency would require primary potentials >300 kV.

Therefore, the assumed primary source for the calculations imposed limitations on the intensity and purity that could be achieved and resulted in the bell-shaped efficiency curve. Calculations indicate that order of magnitude increases in efficiency could be achieved with lower Z targets if the primary source had a bremsstrahlung continuum with light-inherent filtration and operating potentials of 30-60 kV. Similarly, the efficiency of high-Z targets could be improved by a factor of 2 if a primary source with a 500-kV potential were used.

REFERENCES

1. S. K. Allison and W. Duane, "Experimental Determination of the Critical Excitation Frequency for the Production of Fluorescent X-Radiation," Proc. Nat. Acad. Sci. **11**, 485 (1925).

2. A. H. Compton, "The Efficiency of Production of Fluorescent X-Rays," Philos. Mag. **8**, 961 (1929).

3. H. Kustner, "Die Erzeugung Intensiver Monochromatischer Röntgenstrahlen mit Hilfe Technischer Röhren Ohne Spektralapparat," Z. Physik **70**, 324 (1931).

4. T. H. Rogers, "Production of Monochromatic X-Radiation for Microradiography by Excitation of Fluorescent Characteristic Radiation," J. Appl. Phys. **23**, 881 (1952).

5. H. R. Splettstosser and H. E. Seemann, "Application of Fluorescence X-Rays to Metallurgical Microradiography," J. Appl. Phys. **23**, 1217 (1952).

6. J. L. Gaines, P. J. Ebert, and G. R. Leipelt, "Detector Calibration Techniques, X-Ray Machine Intensities and Fluorescent X-Ray Spectrum Catalog," Lawrence Livermore Laboratory report UCID-16091 (November 1967).

7. R. L. Kathren, "Spectral and Output Measurements of a Wide Beam K-Fluorescence Radiator," Lawrence Livermore Laboratory report UCRL-14151 (March 1965).

8. R. L. Kathren, F. L. Rising, and H. V. Larson, "K-Fluorescence X-Rays: a Multi-Use Tool for Health Physics," Health Phys. **21**, 285 (1971).

9. B. J. Krohn, W. B. Chambers, and E. Storm, "The Photon Energy Response of Several Commercial Ionization Chambers, Geiger Counters, and Thermoluminescent Detectors," Los Alamos Scientific Laboratory report LA-4052 (February 1969).

10. H. V. Larson, J. T. Myers, and W. C. Roesch, "Wide-Beam Fluorescent X-Ray Source," Nucleonics **13**, 100 (1955).

11. J. H. McCrary, L. H. Ziegler, and L. D. Looney, "Calibration and Use of the 75-kVP X-Ray Facility," EG&G reports L-229 (1968) and L-940 (1969).

12. H. E. Seemann, "Spectral Sensitivity of Two Commercial X-Ray Films between 0.2 and 2.5 Angstroms," Rev. Sci. Instr. **21**, 314 (1950).

13. E. Storm and S. Shlaer, "Development of Energy-Independent Film Badges with Multi-Element Filters," Health Phys. **11**, 1127 (1965).

14. E. F. Kaelble, *Handbook of X-Rays* (McGraw-Hill Book Co., New York, 1967), Part 4.

15. E. Storm, H. I. Israel, and D. W. Lier, "X-Ray Spectral Distributions from Thick Tungsten Targets in the Energy Range 12 to 300 kV," *Advances in X-Ray Analysis* (Plenum, New York, 1971) Vol. 15, p. 339.

16. H. I. Israel, D. W. Lier, and E. Storm, "Comparison of Detectors Used in the Measurement of 10 to 300 keV X-Ra Spectra," Nucl. Instr. Meth. **91**, 141 (1971).

17. E. Storm, "Calculated Bremsstrahlung Spectra from Thick Tungsten Targets," Phys. Rev. **A5**, 2328 (1972).

18. E. Storm, "Emission of Characteristic L and K Radiation from Thick Tungsten Targets," J. Appl. Phys. **43**, 2790 (1972).

19. D. T. Cromer, to be published in Acta Crystallographica.

20. D. T. Cromer and J. B. Mann, "Compton Scattering Factors for Spherically Symmetric Free Atoms," J. Chem. Phys. **47**, 1892 (1967).

21. D. T. Cromer, "Compton Scattering Factors for Aspherical Free Atoms," J. Chem. Phys. **50**, 4857 (1969).

22. E. Storm and H. I. Israel, "Photon Cross Sections from 1 keV to 100 MeV for Elements Z = 1 to Z = 100," Nucl. Data Tables A7, 565 (1970).

☆ U.S. GOVERNMENT PRINTING OFFICE: 1976—777-018/1